Seasonality in Arctic Warming Driven by Sea Ice Effective Heat Capacity

LILY C. HAHN,[a] KYLE C. ARMOUR,[a,b] DAVID S. BATTISTI,[a] IAN EISENMAN,[c] AND CECILIA M. BITZ[a]

[a] *Department of Atmospheric Sciences, University of Washington, Seattle, Washington*
[b] *School of Oceanography, University of Washington, Seattle, Washington*
[c] *Scripps Institution of Oceanography, University of California San Diego, La Jolla, California*

(Manuscript received 14 August 2021, in final form 11 November 2021)

ABSTRACT: Arctic surface warming under greenhouse gas forcing peaks in winter and reaches its minimum during summer in both observations and model projections. Many mechanisms have been proposed to explain this seasonal asymmetry, but disentangling these processes remains a challenge in the interpretation of general circulation model (GCM) experiments. To isolate these mechanisms, we use an idealized single-column sea ice model (SCM) that captures the seasonal pattern of Arctic warming. SCM experiments demonstrate that as sea ice melts and exposes open ocean, the accompanying increase in effective surface heat capacity alone can produce the observed pattern of peak warming in early winter (shifting to late winter under increased forcing) by slowing the seasonal heating rate, thus delaying the phase and reducing the amplitude of the seasonal cycle of surface temperature. To investigate warming seasonality in more complex models, we perform GCM experiments that individually isolate sea ice albedo and thermodynamic effects under CO_2 forcing. These also show a key role for the effective heat capacity of sea ice in promoting seasonal asymmetry through suppressing summer warming, in addition to precluding summer climatological inversions and a positive summer lapse-rate feedback. Peak winter warming in GCM experiments is further supported by a positive winter lapse-rate feedback, due to cold initial surface temperatures and strong surface-trapped warming that are enabled by the albedo effects of sea ice alone. While many factors contribute to the seasonal pattern of Arctic warming, these results highlight changes in effective surface heat capacity as a central mechanism supporting this seasonality.

SIGNIFICANCE STATEMENT: Under increasing concentrations of atmospheric greenhouse gases, the strongest Arctic warming has occurred during early winter, but the reasons for this seasonal pattern of warming are not well understood. We use experiments in both simple and complex models with certain sea ice processes turned on and off to disentangle potential drivers of seasonality in Arctic warming. When sea ice melts and open ocean is exposed, surface temperatures are slower to reach the warm-season maximum and slower to cool back down below freezing in early winter. We find that this process alone can produce the observed pattern of maximum Arctic warming in early winter, highlighting a fundamental mechanism for the seasonality of Arctic warming.

KEYWORDS: Arctic; Climate change; Climate models; Sea ice; Seasonal cycle

1. Introduction

In both observations and model simulations, recent Arctic surface warming has outpaced the global average by a factor of more than 2 (Screen and Simmonds 2010a; Serreze et al. 2009). While sea ice melt and the ice-albedo feedback peak during summer, the strongest Arctic warming is observed several months later during early winter (Screen and Simmonds 2010b). This seasonal asymmetry is also found in model projections, from the earliest model generations to the newest iteration of climate models in phase 6 of the Coupled Model Intercomparison Project (CMIP6) (Deser et al. 2010; Hahn et al. 2021; Holland and Bitz 2003; Manabe and Stouffer 1980). Figure 1 illustrates the seasonal pattern of Arctic warming within the fully coupled Community Earth System Model version 2 (CESM2) (Danabasoglu et al. 2020). While consistent with other CMIP6 models in producing winter-amplified Arctic warming, this model's 1pctCO2–4xext experiment illustrates a full range of annually ice-covered, seasonally ice-free, and annually ice-free conditions. In this experiment, a 1% yr^{-1} increase in atmospheric CO_2 is applied up to a quadrupling of preindustrial concentrations in year 140, with constant CO_2 forcing thereafter. The evolving seasonal cycle of near-surface air temperature (TAS) area-averaged over nonland surfaces from 70° to 90°N in this experiment (Fig. 1a) and the change in TAS with respect to a preindustrial control (piControl) experiment with greenhouse gas concentrations from the year 1850 (Fig. 1b) show several key features: 1) stronger warming during winter than summer, 2) peak warming in early winter for the first 150 years of the experiment, and 3) a shift to peak warming in late winter for higher global warming levels later in the experiment, once early winter temperatures exceed the freezing point. While these features suggest that sea ice loss plays a key role in setting the seasonal pattern of near-surface Arctic warming, they raise the question of how this pattern is produced.

Commonly proposed mechanisms linking sea ice loss to seasonal asymmetry in Arctic warming include 1) the delayed

Supplemental information related to this paper is available at the Journals Online website: https://doi.org/10.1175/JCLI-D-21-0626.s1.

Corresponding author: Lily C. Hahn, lchahn@uw.edu

DOI: 10.1175/JCLI-D-21-0626.1

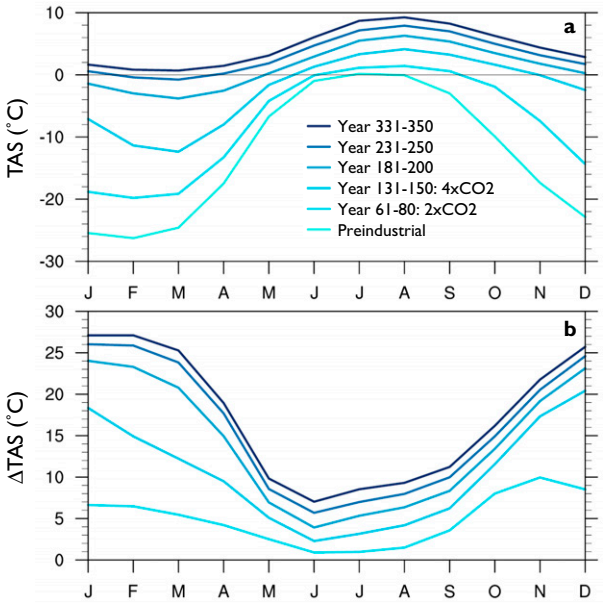

FIG. 1. (a) Near-surface air temperature (TAS; °C) over nonland surfaces from 70° to 90°N in a 350-yr-long 1% yr^{-1} CO_2 ramping experiment (1pctCO2–4xext) in CESM2 and a 150-yr-long preindustrial control (piControl) experiment from which it was initialized; averages are taken over years 1–150 of the piControl experiment and over selected 20-yr periods of the 1pctCO2–4xext experiment, with years 61–80 centered on the time of CO_2 doubling and years 131–150 centered on the time of CO_2 quadrupling. (b) TAS anomalies for each period in the 1pctCO2–4xext experiment calculated relative to the piControl experiment.

warming effect, in which increased surface solar absorption due to reduced summer ice cover contributes to seasonal ocean heat storage and its release to the atmosphere in winter, and 2) the ice insulation effect, in which reduced sea ice thickness and extent allow for stronger heat transfer from the relatively warm upper ocean to the colder atmosphere above particularly during winter, when the air–sea temperature difference is greatest (Deser et al. 2010; Manabe and Stouffer 1980; Screen and Simmonds 2010b). Seasonality in Arctic warming has also been attributed to longwave cloud and temperature feedbacks, including the lapse-rate and Planck feedbacks (Bintanja and van der Linden 2013; Henry and Vallis 2021; Lu and Cai 2009; Pithan and Mauritsen 2014; Sejas et al. 2014; Yoshimori et al. 2014). A positive winter lapse-rate feedback in the Arctic results from surface-trapped warming, which produces weaker longwave emission to space than a vertically uniform atmospheric warming. As this surface-trapped warming is supported by a stable lower troposphere that inhibits vertical mixing, stronger stability in winter promotes a winter-peaking Arctic lapse-rate feedback (Cronin and Jansen 2016; Hahn et al. 2020; Payne et al. 2015). Seasonality in the Planck feedback would also contribute to greater warming in winter than in summer due to a weaker increase in outgoing longwave radiation for a surface warming at initially colder temperatures (Henry and Vallis 2021; Pithan and Mauritsen 2014).

Many of these mechanisms are interconnected, making it difficult to distinguish their relative importance for seasonality in Arctic warming. After seasonal ocean heat storage, the lapse-rate feedback is the second largest contributor to seasonal asymmetry in Arctic warming for models in phases 5 and 6 of the Coupled Model Intercomparison Project (Hahn et al. 2021; Pithan and Mauritsen 2014). Bintanja et al. (2011) and Hahn et al. (2020) suggest that the polar lapse-rate feedback depends on the base-state inversion strength, which itself depends on the existence of sea ice, poleward atmospheric heat transport, and atmospheric emissivity (Cronin and Jansen 2016; Payne et al. 2015; Pithan et al. 2014). More recently, Boeke et al. (2021) find that while inversions are necessary for a positive lapse-rate feedback, this feedback depends more strongly on the amount of surface warming than on the degree of stable stratification. As a result, a more-positive lapse-rate feedback in winter could result from any process that promotes stronger bottom-heavy atmospheric warming, including the ice-albedo feedback (Feldl et al. 2017; Graversen et al. 2014). Dai et al. (2019) and Chung et al. (2021) further suggest that seasonal ocean heat storage and sea ice insulation loss are necessary to kick-start the winter lapse-rate feedback via increased turbulent heat release to the atmosphere over newly opened ocean. Separating these potentially interdependent ice-albedo, seasonal ocean heat storage, and insulation effects of sea ice loss and their impact on the lapse-rate feedback remains a challenge in comprehensive climate models.

An additional mechanism that has received less attention is the idea that changes in the effective heat capacity of the surface layer in the Arctic are responsible for winter-amplified Arctic warming (Dwyer et al. 2012; Robock 1983). As in Dwyer et al. (2012), here we use the term "effective heat capacity" to refer to the thermal inertia of the layer of material (e.g., sea ice, ocean) that sets the surface temperature response to surface heat fluxes. Turbulent mixing in the ocean mixed layer couples a thick layer of water to surface heat fluxes, giving the surface ocean a relatively large effective heat capacity. As a result, ocean surface temperatures respond slowly to surface heat fluxes and with a smaller amplitude than temperatures over land, where a much thinner surface layer responds more quickly and strongly. Meanwhile, the effective heat capacity of sea ice depends on whether it is melting or at temperatures below freezing. At the melting point, sea ice has a large effective heat capacity because surface heat fluxes go toward latent heating to melt ice rather than raising the surface temperature; melting sea ice thus acts like a very deep ocean mixed layer. However, frozen sea ice has a small effective heat capacity because surface heat fluxes go directly toward changing its surface temperature; frozen sea ice acts like a shallow ocean mixed layer or a land-like surface. As frozen sea ice warms to the melting point and then, ultimately, melts completely to expose open ocean, the effective heat capacity of the surface increases. This slows the seasonal rate of warming and cooling and thereby delays the phase and reduces the amplitude of the seasonal cycle of surface temperature. As shown in Dwyer et al. (2012) for CMIP3 models, this phase delay and amplitude reduction has also been found in earlier model generations (Manabe and Stouffer 1980; Mann and Park 1996) and is consistent with the warming pattern shown in Fig. 1. For a doubling of CO_2, the large effective heat capacity of melting ice suppresses summer warming, supporting a winter warming maximum. Under increased forcing, the amplitude reduction from

frozen sea ice to open ocean supports a large difference between very cold winters over ice and warmer winters over ocean, contributing to peak winter warming. Peak warming specifically in early winter is supported by the phase delay in ocean temperatures, which are slower than a frozen ice surface to warm to the seasonal maximum and to cool back below freezing. As a result, the transition from frozen sea ice to open ocean under increased forcing and the accompanying warming maximum occurs first in early winter before shifting to late winter.

The changes in surface effective heat capacity described above are one of several potential explanations for seasonality in Arctic warming that have been generated by diagnostic analysis of CO_2 forcing experiments in comprehensive general circulation models (GCMs). To disentangle these interconnected effects of sea ice loss, here we employ an idealized single-column sea ice model (SCM) in addition to a GCM with certain sea ice processes turned on and off. SCM experiments enable us to separate drivers of seasonality in Arctic warming, particularly the role of effective heat capacity changes alone, while GCM experiments offer insight into additional processes not included in the SCM, such as the lapse-rate feedback. Complementary to previous studies that have isolated the albedo effects of sea ice using experiments with locked or unlocked albedo changes (Feldl et al. 2017; Graversen et al. 2014), we isolate the role of non-albedo sea ice thermodynamics by comparing experiments with identical surface albedo changes, but with sea ice turned on or off. Both the simple SCM and more complex GCM reveal a fundamental role of increasing effective heat capacity in producing seasonality in Arctic warming, as the surface layer shifts from sea ice below the freezing point to melting ice and open ocean. The results also highlight the role of sea ice effective heat capacity for inhibiting a positive summertime lapse-rate feedback, which additionally supports a winter warming maximum.

2. Seasonal asymmetry in a single-column sea ice model

a. Model description

We employ an idealized SCM of the sea ice–ocean–atmosphere system to investigate different mechanisms that have been proposed to cause seasonality in Arctic warming. We use the SCM developed and described by Eisenman and Wettlaufer (2009), which includes an idealized version of the Maykut and Untersteiner (1971) sea ice thermodynamic equations and an idealized atmosphere. The SCM equations are repeated below, with model parameter values listed in Table S1 in the online supplemental material. This model evolves the surface enthalpy E, which represents the latent energy of sea ice or, when no ice is present, the sensible energy of the ocean mixed layer:

$$E = \begin{cases} -L_i H_i, & E < 0 \,(\text{sea ice}) \\ c_{\text{ml}} H_{\text{ml}} T_{\text{ml}}, & E > 0 \,(\text{ocean}) \end{cases}, \tag{1}$$

where L_i is the latent heat of fusion for sea ice, H_i is the sea ice thickness, c_{ml} is the specific heat capacity of the ocean mixed layer, H_{ml} is depth of the ocean mixed layer (50 m), and T_{ml} is the mixed layer temperature departure from the freezing point, which is 0°C in this model. Note that E evolves in response to the net surface energy flux, which includes solar forcing as a function of the insolation $F_s(t)$ and surface albedo $\alpha(E)$, a linearized representation of outgoing longwave radiation (OLR), basal heat flux F_B, sea ice export, and climate forcing ΔF_0, which can be varied from 0 to represent an increase in atmospheric CO_2:

$$\frac{dE}{dt} = \underbrace{[1 - \alpha(E)]F_S(t)}_{\text{solar}} \underbrace{- F_0(t) - F_T(t)T(t,E)}_{\text{OLR}} + \underbrace{F_B}_{\text{basal heat flux}} + \underbrace{\upsilon_0 R(-E)}_{\text{ice export}} + \underbrace{\Delta F_0}_{\text{forcing}}. \tag{2}$$

The prescribed values of $F_S(t)$, $F_0(t)$, and $F_T(t)$ vary seasonally, while F_B and ΔF_0 are annually constant. The $F_0(t)$ and $F_T(t)$ values have been derived as a function of atmospheric opacity, including the effects of climatological Arctic cloud cover (Maykut and Church 1973), and atmospheric heat transport to the Arctic, which is based on observations of surface air temperature to the south of the Arctic (Kalnay et al. 1996; Nakamura and Oort 1988). Central Arctic values from Maykut and Untersteiner (1971) are prescribed for $F_S(t)$ and F_B. In the ice export term, $\upsilon_o = 10\%\ \text{yr}^{-1}$, and the linear ramp function $R(-E)$ is equal to $-E$ when ice is present ($E \le 0$) and zero when there is no ice ($E > 0$).

When ice is present, the surface temperature T is calculated using a balance between the surface energy flux and the upward heat flux through the ice: $-[1 - \alpha(E)]F_s(t) + F_0(t) + F_T(t)T^*(t,E) - \Delta F_0 = -k_i T^*(t,E)/H_i = k_i L_i T^*(t,E)/E$, where k_i is the thermal conductivity of sea ice and T^* is the surface temperature satisfying this balance. When this balance gives surface temperatures below freezing ($T^* < 0$), T is set to T^*. When this balance gives surface temperatures above freezing ($T^* > 0$) while ice is still present ($E < 0$), T is fixed at the freezing point (0°C) while the ice melts. Once the ocean is ice-free ($E > 0$), T equals the enthalpy of the mixed layer divided by its effective heat capacity. The surface temperature for these three regimes is given by

$$T(t,E) = \begin{cases} -\dfrac{(1-\alpha_i)F_s(t) - F_0(t) + \Delta F_0}{k_i L_i/E - F_T(t)}, & E < 0,\ T^* < 0 \quad \text{(frozen ice)}, \\ 0, & E < 0,\ T^* > 0 \quad \text{(melting ice)}, \\ \dfrac{E}{c_{\text{ml}} H_{\text{ml}}}, & E \ge 0 \quad \text{(open ocean)}. \end{cases} \tag{3}$$

The albedo $\alpha(E)$ transitions smoothly from ice ($\alpha_i = 0.68$) to ocean ($\alpha_{\text{ml}} = 0.2$) with a characteristic smoothness set by $H_\alpha = 0.5$ m:

$$\alpha(E) = \frac{\alpha_{\text{ml}} + \alpha_i}{2} + \frac{\alpha_{\text{ml}} - \alpha_i}{2} \tanh\left(\frac{E}{L_i H_\alpha}\right). \tag{4}$$

b. Seasonal pattern of warming in the SCM

To assess the extent to which this simple model can reproduce the pattern of seasonality in Arctic warming

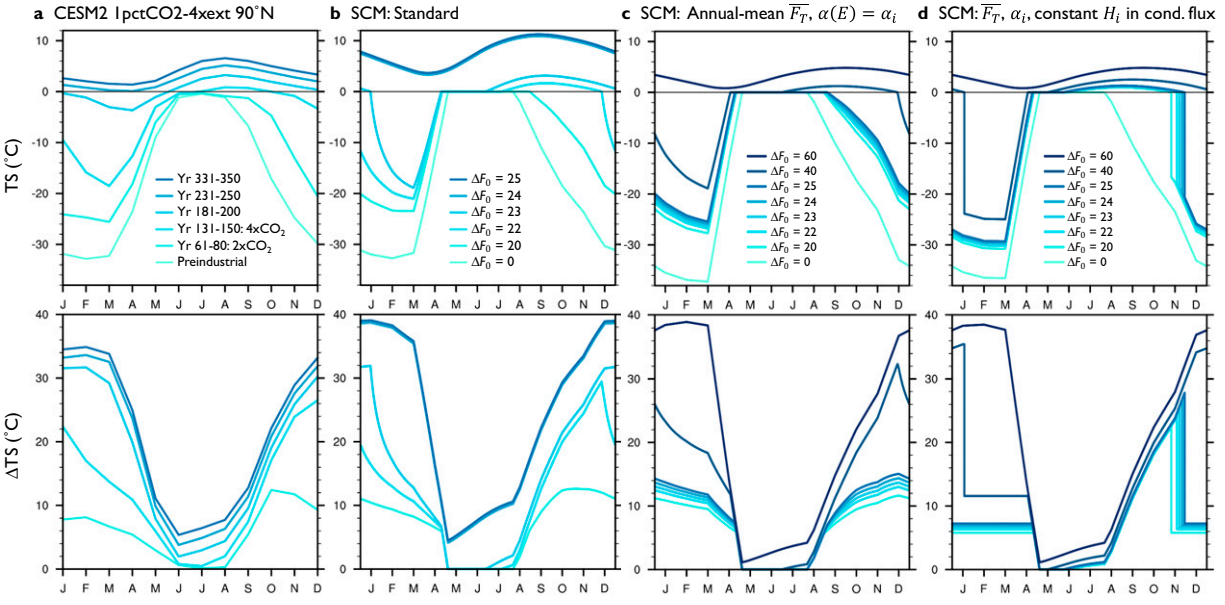

FIG. 2. (top) Surface temperature (TS; °C) for (a) the 1pctCO2–4xext and piControl experiments at 90°N in CESM2, and for surface forcing experiments in (b) the standard SCM, (c) the SCM with annual-mean $F_T(t)$ and constant $\alpha(E) = \alpha_i$, and (d) the SCM with annual-mean $F_T(t)$, constant $\alpha(E) = \alpha_i$, and constant ice thickness H_i when calculating the conductive heat flux through frozen ice, which is set to the annual-mean H_i from the $\Delta F_0 = 0$ experiment with annual-mean $F_T(t)$ and constant $\alpha(E) = \alpha_i$. (bottom) TS anomalies compared to preindustrial CO_2 (for CESM2) or $\Delta F_0 = 0$ (for the SCM).

found in more complex models and observations, we compare steady-state solutions under varying degrees of forcing in the SCM with CESM2 preindustrial control and 1pctCO2–4xext experiments (Figs. 2a,b). These CESM2 experiments are identical to those displayed in Fig. 1, but Fig. 2a shows surface temperature for 90°N rather than near-surface temperature for 70°–90°N for better comparison with the SCM, which models surface temperature using observationally based parameters for the central Arctic. The bottom row in Fig. 2 shows surface temperature anomalies for climate forcing experiments with respect to experiments with preindustrial CO_2 (for CESM2) or $\Delta F_0 = 0$ (for the SCM).

The SCM experiment with $\Delta F_0 = 0$ produces a similar seasonal cycle to CESM2 under preindustrial conditions. Greater climate forcing is required to produce a given warming in the SCM because it excludes many of the climate feedbacks in CESM2; rather than show equivalent forcings for both models, we include forcings that illustrate the full range of responses: annually ice-covered, seasonally ice-free, and annually ice-free conditions. Despite neglecting many processes that additionally impact surface temperature, the SCM captures the key features of seasonality in Arctic warming found in CESM2. This includes 1) enhanced warming in winter compared to summer, 2) asymmetry in winter warming, with peak warming initially occurring in early winter, and 3) a shift to peak warming in late winter with greater forcing, once early winter temperatures exceed the freezing point. This warming pattern can also be described as a phase delay and amplitude reduction in the surface temperature as the surface layer shifts from perennial sea ice cover to seasonally and annually ice-free conditions.

c. Causes of seasonal warming asymmetry in the SCM

With the SCM capturing the seasonal pattern of Arctic warming found in observations and more complex models, we next investigate factors contributing to this pattern in this model. The SCM includes a representation of several mechanisms that have been suggested to contribute to seasonality in Arctic warming: seasonally varying Planck and surface-albedo feedbacks, changes in ice insulation and conductive heat flux as sea ice thins, and changes in surface effective heat capacity as sea ice melts and exposes open ocean. Lapse-rate, cloud, and water vapor feedbacks and changes in poleward heat transport are not included in the SCM, but are later explored in GCM experiments (section 3) and by incorporating a lapse-rate feedback parameterization into the SCM (section 2f).

The surface albedo and Planck feedbacks both contribute to seasonal warming asymmetry in the SCM. Enthalpy maximizes at the end of summer and increases most at this time under forcing, yielding a late summer maximum in the positive albedo feedback. The Planck feedback, equal to $-F_T(t)$ in the SCM, is a function of observations of climatological Arctic cloud fraction (Maykut and Church 1973), which reach a maximum in September, producing a less-negative Planck feedback in fall and early winter than in late winter. While nonlinearity in the Stefan–Boltzmann equation may also promote seasonality in the Planck feedback and amplify cold-season warming in GCMs (Henry and Vallis 2021; Pithan and Mauritsen 2014), the linearized Planck response in the SCM

contributes to seasonality in warming only as a result of seasonality in climatological atmospheric opacity. For comparison with the SCM, we estimate $F_T(t)$ from a CESM preindustrial control experiment, described in section 3, using a linear regression of OLR and surface temperature for nonland grid points north of 70°N. This GCM-derived $F_T(t)$ has a similar seasonal structure to that in the SCM, with maximum OLR in March and minimum OLR in September supporting enhanced warming in fall and early winter.

The early winter warming maximum in the SCM is dampened when either an annual-mean Planck feedback ($\overline{F_T}$) or constant ice albedo [$\alpha(E) = \alpha_i$] is implemented (Fig. S1), with the combined influence of these changes shown in Fig. 2c. Comparison of Figs. 2b and 2c illustrates that the seasonally varying Planck feedback and particularly the albedo feedback reduce the amount of forcing necessary to support a transition to open ocean in early winter and an associated increase in early winter warming. However, seasonal asymmetry in warming persists even in the absence of seasonal asymmetry in feedbacks (Fig. 2c), suggesting that the warming maximum in early winter (and in late winter under increased forcing) is a fundamental property of warming with sea ice loss. Greater forcing is required to transition to open ocean in Fig. 2c, primarily due to the elimination of the albedo feedback; additional experiments prescribing the annual-mean albedo from each forcing experiment with annual-mean $F_T(t)$ (thus maintaining an annual-mean albedo feedback rather than constant ice albedo) require forcing more comparable to the standard SCM and similarly produce a winter warming maximum in the absence of feedback seasonality (Fig. S2).

We next explore seasonality in warming contributed by changes in the conductive heat flux through sea ice ($-k_iT/H_i$), which maximizes in early winter as a result of both thinner ice and colder surface temperatures, and increases with increased forcing as ice thins. To illustrate the effects of seasonality in conductive heat flux and its increase with forcing, we compare the SCM with an annual-mean Planck feedback and constant ice albedo [$\overline{F_T}$ and $\alpha(E) = \alpha_i$; see Fig. 2c] to the same SCM, but with a constant ice thickness H_i used when calculating the conductive heat flux through frozen ice (Fig. 2d). This constant H_i is set to the annual-mean ice thickness from the $\Delta F_0 = 0$ experiment with $\overline{F_T}$ and $\alpha(E) = \alpha_i$ ($H_i = 3.2$ m). With constant ice thickness in the conductive heat flux, warming for a given forcing is identical in all months with frozen ice (Fig. 2d). This illustrates that seasonality in conductive heat flux and its increase with forcing contribute to peak warming in early winter over frozen ice (Fig. 2c). Additional experiments separating the role of annual-mean ice thinning and seasonality in ice thinning for conductive heat flux and surface warming demonstrate that annual-mean thinning enhances winter warming to a greater degree than seasonality in thinning, which contributes to stronger warming in early winter and weaker warming in late winter over frozen ice (Fig. S3a). In addition to enhanced warming over frozen ice, winter warming as ice transitions to open ocean is also strengthened by starting from very cold surface temperatures as a result of limited conductive heat flux through thick ice; this warming is weakened when a thinner base-state ice depth is prescribed in the conductive heat flux (Figs. S3b,c). The dependence of conductive heat flux on sea ice thickness thus contributes to greater winter warming both over frozen ice and for the transition to open ocean.

Importantly, even with seasonally constant warming over frozen ice in Fig. 2d, the transition from frozen ice to seasonally ice-free ocean with increased forcing produces an early winter warming maximum, and the transition from seasonally to annually ice-free conditions produces a late winter warming maximum. This intrinsic link between the ice–ocean transition and peak Arctic warming, even in the absence of seasonal variations in feedbacks or insulation effects, suggests that the seasonal pattern of warming fundamentally stems from changes in the effective heat capacity of these surface types (Dwyer et al. 2012; Manabe and Stouffer 1980; Mann and Park 1996). As frozen sea ice transitions to open ocean in fall and early winter with increased forcing, the greater effective heat capacity of the ocean mixed layer slows seasonal warming in summer and slows cooling back below freezing in early winter, supporting a large increase in early winter temperatures relative to the much colder temperatures of frozen ice under control forcing.

d. Contribution of effective heat capacity changes to the seasonal pattern of Arctic warming

We further investigate the role of effective heat capacity for seasonality in Arctic warming by explicitly modeling effective heat capacity changes in the SCM, and compare the results with an analytical solution based on Dwyer et al. (2012). Dwyer et al. illustrate heat capacity effects on seasonality using a simple energy balance model,

$$C\frac{dT}{dt} = Q(t) - \beta T(t), \tag{5}$$

where C is effective heat capacity, $T(t)$ is surface temperature, $Q(t)$ is the seasonally varying surface forcing independent of temperature (including solar forcing), and β is a constant, with $-\beta T(t)$ representing damping of the surface temperature response (including through OLR changes). This gives the following phase and amplitude relationships between the surface forcing, $Q_o\cos(\omega t - \phi_Q)$, and the surface temperature, $T(t) = T_o\cos(\omega t - \phi_T)$ with $\omega = 2\pi\,\mathrm{yr}^{-1}$:

$$\phi_T - \phi_Q = \arctan\frac{\omega C}{\beta}, \tag{6}$$

$$T_o = \frac{Q_o}{\sqrt{\beta^2 + \omega^2 C^2}}. \tag{7}$$

In the limit of small effective heat capacity ($C \to 0$), there is no phase lag between $Q(t)$ and surface temperature, while a much larger effective heat capacity ($C \to \infty$) gives a maximum phase delay of 90°, or three months for an annual harmonic forcing. A transition from frozen ice to open ocean with increased forcing would cause an increase in effective heat capacity and thus a phase delay [Eq. (6)] and amplitude reduction [Eq. (7)] in surface temperature, consistent with the SCM response in Fig. 2d.

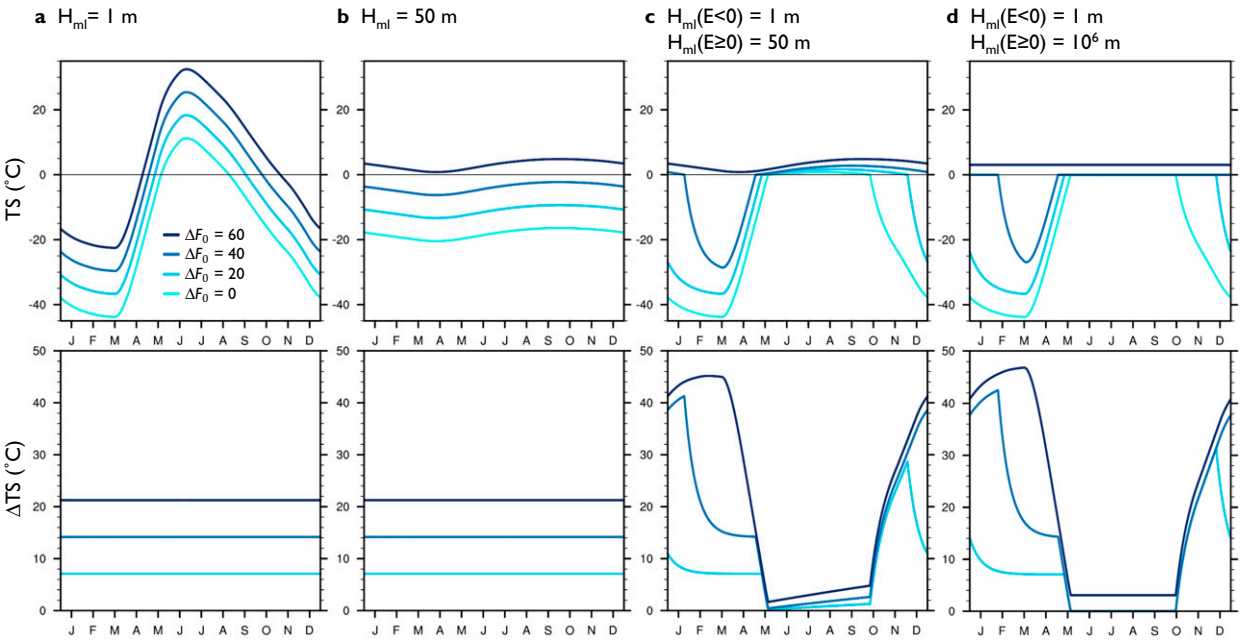

FIG. 3. (top) Surface temperature (TS; °C) for various surface forcings and mixed layer depths in the SCM run as a mixed layer with annual-mean $F_T(t)$ and constant $\alpha(E) = \alpha_i$. (bottom) TS anomalies for each forcing experiment compared to $\Delta F_0 = 0$.

To explicitly model the effect of heat capacity differences between frozen ice, melting ice, and open ocean, we run the SCM as an ocean mixed layer (without a representation of sea ice), the effective heat capacity of which can be modified by changing the mixed layer depth ($C = c_{ml}H_{ml}$). Without sea ice in this version of the model, Eq. (3) becomes $T(t, E) = E/c_{ml}H_{ml}$, ice export is set to zero, and there is no conductive heat flux. As above, we also apply an annual-mean Planck feedback and constant ice albedo [$\overline{F_T}$ and $\alpha(E) = \alpha_i$] in order to isolate the impact of heat capacity changes alone on seasonality in Arctic warming. We perform four sets of experiments with this SCM: 1) using a mixed layer depth of H_{ml} = 1 m (representing the small effective heat capacity of frozen ice); 2) using a mixed layer depth of H_{ml} = 50 m (representing the large effective heat capacity of open ocean); 3) using a variable mixed layer depth that is H_{ml} = 1 m when the surface temperature is below freezing, defined by $E < 0$ (representing the small effective heat capacity of frozen ice) and becomes H_{ml} = 50 m when the surface temperature is at or above the melting point, defined by $E \geq 0$ (representing the large effective heat capacity of open ocean); and 4), as in method 3 but using $H_{ml} = 10^6$ m when $E \geq 0$ (representing the very large effective heat capacity associated with the latent energy sink of sea ice melting at a nearly constant temperature).

Consistent with Eqs. (6) and (7), SCM experiment 2 with a deep mixed layer representing open ocean shows a delayed phase and reduced amplitude in surface temperature (Fig. 3b) compared to experiment 1 with a shallow mixed layer representing frozen ice (Fig. 3a), while both experiments show a seasonally uniform warming in response to forcing. In experiment 3, which allows a transition from the effective heat capacity of frozen ice for $E < 0$ to that of ocean when $E \geq 0$ (Fig. 3c), an increase in effective heat capacity under forcing produces peak warming in early winter by delaying the phase and reducing the amplitude of surface temperature (Fig. 3c). Under greater forcing, this ice–ocean transition and associated amplitude reduction from colder ice to warmer ocean temperatures occurs later in the year, producing peak warming in late winter. Similarly, experiment 4, which allows a transition from the effective heat capacity of frozen ice for $E < 0$ to the much larger effective heat capacity of melting ice when $E \geq 0$, produces nearly identical results to experiment 3 with an early (shifting to late) winter warming maximum under forcing, in addition to inhibiting summer warming over melting ice (Fig. 3d). In reality, frozen ice would transition to a combination of melting ice in summer and open ocean later in the year, and the much larger effective heat capacity of either of these surface types compared to frozen ice would similarly produce peak early winter warming.

We note that observed Arctic mixed layer depths vary seasonally and spatially, such that a 50-m ocean mixed layer depth is not representative for all times and locations. Nevertheless, we find similar results using a range of ocean mixed layer depths (spanning 8 m to 100 m) when $E \geq 0$ (Fig. S4a), all giving peak early winter warming associated with the transition from the small effective heat capacity of frozen ice to the larger effective heat capacity of open ocean. A thinner ocean mixed layer in summer than winter consistent with Arctic observations (Peralta-Ferriz and Woodgate 2015) would produce a smaller phase lag in ocean temperatures and a slightly earlier winter warming maximum (Fig. S4b). Temperature phasing and the timing of peak warming become less sensitive to ocean mixed layer depth as depth increases, as expected from Eq. (6) and as illustrated by the similarity of

the seasonal warming patterns for the transition from frozen ice [$H_{ml}(E < 0) = 1$ m] to either melting ice [$H_{ml}(E \geq 0) = 10^6$ m] or open ocean [$H_{ml}(E \geq 0) = 50$ m] (Figs. 3c,d). Increasing effective heat capacity from frozen ice to either melting ice or open ocean consistently produces peak early winter warming, with small sensitivity to the exact mixed layer depth of open ocean.

We compare the SCM results to the Dwyer et al. (2012) analytic solution for the expected amplitude and phase shift of surface temperature by applying Eqs. (6) and (7) to the 1- and 50-m mixed layer SCM, where

$$Q(t) = \underbrace{[1 - \alpha_i]F_s(t)}_{\text{solar}} - \underbrace{F_0(t)}_{\text{OLR}} + \underbrace{F_B}_{\text{basal heat flux}} + \underbrace{\Delta F_0}_{\text{forcing}}, \quad (8)$$

$$\beta = F_T(t). \quad (9)$$

Results are similar for the analytic solution (Figs. S5a,b, gray lines) and SCM experiments (Figs. S5a,b, black lines), with small differences due to applying discrete monthly solar forcing and $F_0(t)$ to the SCM. When $F_S(t)$ is instead represented as a cosine function (with phase and amplitude matching the discrete monthly solar forcing) and the annual-mean value of $F_0(t)$ is used, the amplitude and phase shift of surface temperature in the SCM exactly match results from Eqs. (6) and (7) (Figs. S5c,d). These results from the mixed layer SCM and analytic solution demonstrate that the key features of Arctic seasonality in warming can be produced simply by representing how the effective heat capacity of the Arctic surface layer evolves with surface temperature.

e. SCM with and without sea ice thermodynamics

A final way to isolate the role of effective surface heat capacity changes and other thermodynamic processes is to compare SCM experiments with ice to SCM experiments with identical prescribed albedo changes but no ice. Figures 4a–c show the same SCM configurations as in Figs. 2b–d for select forcing experiments illustrating annually ice-covered, seasonally ice-free, and annually ice-free conditions (solid lines; *Ice* experiments). Overlaid are results for the same SCM configurations, but with a 50-m mixed layer SCM with no ice and with prescribed surface albedo from the *Ice* experiments (dashed lines; *No ice*, *set albedo* experiments). With identical albedo changes under increased forcing, these *Ice* and *No ice*, *set albedo* experiments differ only in their inclusion or exclusion of sea ice thermodynamics.

In both the standard SCM (Fig. 4a) and the SCM with an annual-mean Planck feedback and constant ice albedo (Fig. 4b), ice thermodynamics suppress summer warming over melting ice and enhance winter warming. For surface temperatures below freezing, this enhanced winter warming results from increasing conductive heat flux through thinning ice. When ice thickness is kept constant for the conductive heat flux (Fig. 4c), winter warming at temperatures below freezing is instead reduced in the *Ice* experiments compared to the *No ice*, *set albedo* experiments as a result of ice export changes in only the *Ice* experiments. Even with constant ice thickness in the conductive heat flux and reduced winter warming over frozen ice, the transition above freezing temperatures produces enhanced winter warming when ice thermodynamics are included due to a phase delay and amplitude reduction in temperature with increasing effective surface heat capacity. Instead, in the *No ice*, *set albedo* experiment, the constant effective surface heat capacity for the 50-m mixed layer gives seasonally constant warming for all forcings. This illustrates the essential role of sea ice thermodynamics, specifically conductive heat flux changes as frozen ice warms and effective heat capacity changes as frozen ice melts and transitions to open ocean, for the seasonal pattern of Arctic warming.

f. Addition of a lapse-rate feedback to the SCM

Based on analysis of comprehensive GCM experiments, Pithan and Mauritsen (2014) suggest that the winter-peaking lapse-rate feedback is an important driver of seasonality in Arctic warming. To estimate how much additional seasonality in warming the lapse-rate feedback would contribute to the SCM, we add a contribution from this feedback to the surface energy balance, multiplied by the surface warming under forcing compared to $\Delta F_0 = 0$. We calculate the lapse-rate feedback for a doubling of CO_2 compared to preindustrial conditions in CESM slab ocean experiments, described in section 3, for nonland grid points north of 70°N. This gives a fairly constant lapse-rate feedback for grid points with below-freezing surface temperatures under CO_2 doubling, and a weaker lapse-rate feedback for grid points that exceed the freezing point under CO_2 doubling. Since we add a lapse-rate feedback to the SCM in a forcing experiment ($\Delta F_0 = 12$) that does not warm above the freezing point, we apply the CESM lapse-rate feedback averaged only over grid points that remain below freezing under CO_2 doubling to the SCM. We show this $\Delta F_0 = 12$ forcing experiment in the SCM because it produces warming of similar magnitude to the area-averaged nonland Arctic warming in the CESM CO_2 doubling experiments. We apply both an annual-mean lapse-rate feedback (1 W m^{-2} K^{-1}) and a monthly varying lapse-rate feedback (values in Table S1) based on CESM experiments. We note that this addition of a lapse-rate feedback to the SCM is highly simplified, and in reality this feedback depends on the vertical structure of temperature change which itself is a consequence of other feedbacks (Boeke et al. 2021; Feldl et al. 2020; Henry et al. 2021).

Surface temperatures with and without a lapse-rate feedback in the standard SCM are shown in Fig. 5 for $\Delta F_0 = 12$ compared to $\Delta F_0 = 0$. In these experiments, the addition of an annual-mean lapse-rate feedback (dashed line) increases winter warming by about 3 degrees, magnifying the early winter warming maximum that exists in the SCM without the lapse-rate feedback. Introducing seasonality in the lapse-rate feedback (dotted line) contributes additional warming particularly in early winter, but the majority of the winter warming contributed by the lapse-rate feedback in the SCM can be explained by the annual-mean lapse-rate feedback acting on winter-amplified surface warming. Considering the total warming, the majority of seasonality in warming in the SCM

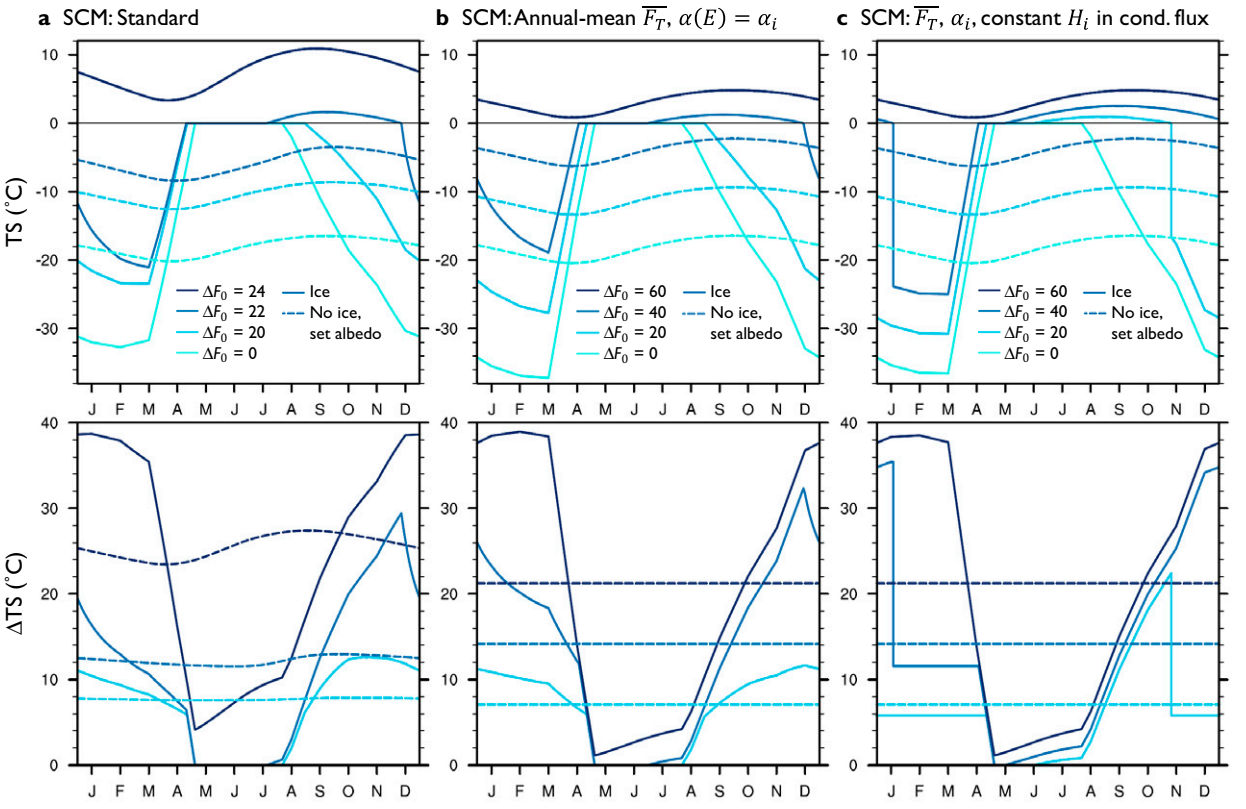

FIG. 4. (top) As in Figs. 2b–d for select surface forcing experiments, solid lines show surface temperature (TS; °C) in (a) the standard SCM, (b) the SCM with annual-mean $F_T(t)$ and constant $\alpha(E) = \alpha_i$, and (c) the SCM with annual-mean $F_T(t)$, constant $\alpha(E) = \alpha_i$, and constant ice thickness H_i when calculating the conductive heat flux through frozen ice, which is set to the annual-mean H_i from the $\Delta F_0 = 0$ experiment with annual-mean $F_T(t)$ and constant $\alpha(E) = \alpha_i$. Dashed lines show TS for identical experiments, but with a mixed layer SCM and prescribed surface albedo from the experiments with ice. (bottom) TS anomalies compared to the $\Delta F_0 = 0$ experiment. Note that TS is identical in the *Ice* and *No ice*, *set albedo* experiments for the highest forcing experiment, which is annually ice-free.

is still due to processes other than the lapse-rate feedback. For this forcing, these processes primarily enhance warming in winter due to an increase in conductive heat flux through thinning ice, and suppress warming in summer due to the large effective heat capacity of melting ice.

3. Seasonality of Arctic warming with and without sea ice in CESM

The above results suggest that in the absence of seasonality in climate feedbacks, seasonality in Arctic warming is fundamentally driven by increasing conductive heat flux through thinning ice and increasing effective heat capacity as ice melts and exposes open ocean. Can we similarly isolate the role of sea ice thermodynamic effects within a GCM? Complementary to previous GCM experiments isolating the impact of sea ice albedo changes on Arctic warming (Feldl et al. 2017; Graversen et al. 2014), here we use idealized GCM experiments to isolate non-albedo thermodynamic effects of sea ice on Arctic warming. While analogous to SCM experiments in section 2e, these GCM experiments enable us to include not only the thermodynamic and climate feedback effects incorporated in the SCM, but also more complex polar climate feedbacks and changes in poleward heat transport that the SCM excludes.

a. CESM experiments

We perform all experiments with the CESM (Hurrell et al. 2013) version 1.2.2, which uses the Community Atmosphere Model version 4 (CAM4; Neale et al. 2013) with a horizontal resolution of 0.9° × 1.25° and 26 vertical levels, the Community Land Model version 4 (CLM4; Oleson et al. 2010) and the Los Alamos Sea Ice Model version 4 (CICE4; Hunke and Lipscomb 2008). For these experiments, CAM4 is coupled to a slab ocean model (SOM) with a prescribed, spatially heterogeneous monthly climatology of ocean heat flux convergence and an annual-mean, spatially variable mixed layer depth taken from a fully coupled preindustrial control simulation (Bitz et al. 2012). While all CESM SOM experiments have been run with the elevation of Antarctica flattened to 0 m above sea level, this flattening has a negligible impact on Arctic surface temperatures (Hahn et al. 2020), which are the focus here.

For all configurations of CESM, CO_2 is abruptly doubled from preindustrial concentrations before running each simulation for 50 years, with climatologies calculated over the final

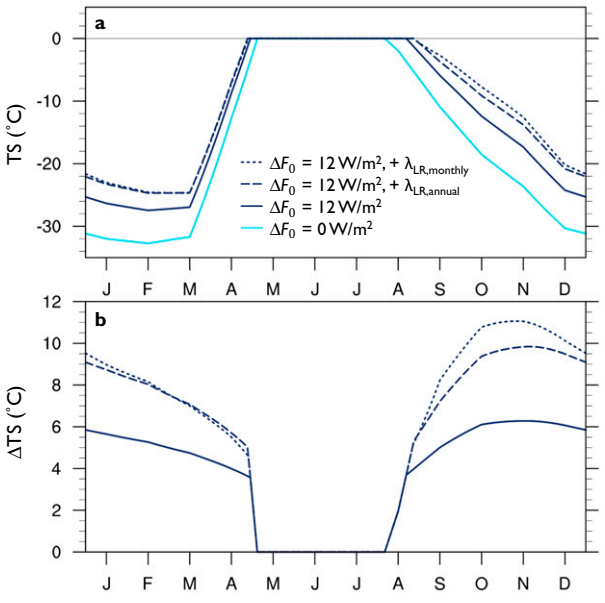

FIG. 5. (a) Surface temperature (TS; °C) and (b) anomalies in TS for $\Delta F_0 = 12$ compared to $\Delta F_0 = 0$ in the standard SCM (solid lines) and the standard SCM with the addition of a simple annual-mean (dashed line) or monthly mean (dotted line) lapse-rate feedback.

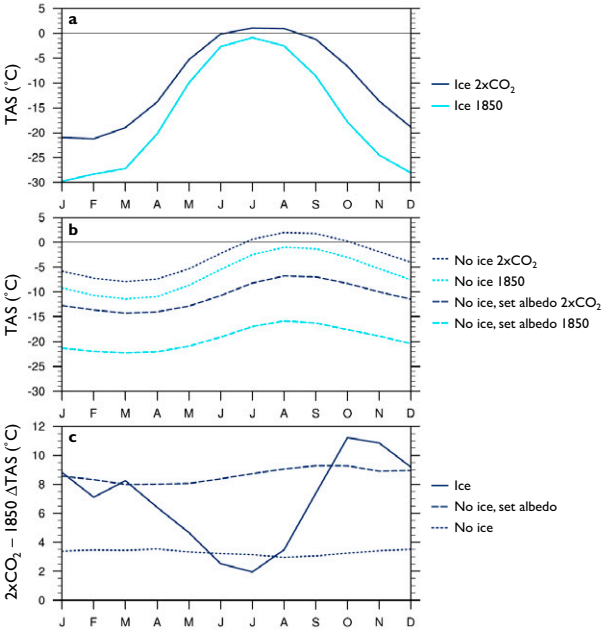

FIG. 6. Near-surface temperature (TAS; °C) over nonland surfaces from 70° to 90°N for the CESM SOM (a) *Ice* experiment and (b) *No ice* and *No ice*, *set albedo* experiments under preindustrial (light blue) and doubled CO_2 (dark blue). (c) TAS anomalies for doubled CO_2 compared to preindustrial experiments (e.g., *Ice* = *Ice* 2xCO_2 minus *Ice* 1850; *No ice* = *No ice* 2xCO_2 minus *No ice* 1850).

30 years, which are near equilibrium. We compare control experiments including full sea ice thermodynamics (called *Ice*) to experiments with no sea ice, in which ocean temperatures can cool below the freezing point (called *No ice*). As in the SCM, we also run experiments with no sea ice in which we prescribe monthly climatological albedo values over nonland surfaces taken from the *Ice* experiments (called *No ice*, *set albedo*). In these *No ice*, *set albedo* experiments, the nonland albedo change under CO_2 doubling is by design almost identical to the *Ice* experiments (<0.7% difference for 70°–90°N). Small differences may result from the way we prescribe albedo, using the climatological fraction of incoming visible solar radiation that is reflected at the surface in the *Ice* experiment to prescribe direct and diffuse, visible and near-infrared surface albedos in the *No ice*, *set albedo* experiment, with zero albedo change by default when there is no sunlight.

With nearly identical albedo changes under CO_2 doubling in the *Ice* and *No ice*, *set albedo* experiments, differences between these experiments reflect non-albedo thermodynamic effects of sea ice. All remaining figures are shown for the Arctic from 70° to 90°N over nonland surfaces.

b. *Impact of sea ice thermodynamics and albedo on Arctic warming*

Including sea ice thermodynamics supports colder winters and warmer summers for the *Ice* (Fig. 6a) compared to *No ice*, *set albedo* (Fig. 6b) experiments. This is consistent with the small effective heat capacity of ice below freezing compared to open ocean, which gives a larger seasonal amplitude and earlier phasing in near-surface temperature in the *Ice* experiments. As in the fully coupled CESM2 (Fig. 1), the CESM SOM *Ice* experiments simulate a summer minimum and early winter maximum in near-surface warming under CO_2 doubling (Fig. 6c). In contrast, warming is nearly constant year-round in experiments without sea ice. The main effect of ice albedo changes (*No ice*, *set albedo* compared to *No ice*) is to strengthen warming in the annual mean, with a slightly greater increase in fall warming than the rest of the year. The main impact of sea ice thermodynamic effects (*Ice* compared to *No ice*, *set albedo*) is to reduce summer warming, as also seen in SCM experiments. Including thermodynamic effects also slightly increases early winter warming, although winter warming is more comparable for *Ice* compared to *No ice*, *set albedo* experiments in the GCM than in the SCM. In addition to the SCM and GCM experiments shown in this study, experiments isolating the impact of sea ice thermodynamics in a moist energy balance model and idealized moist GCM (Feldl and Merlis 2021) produce similar results; ice thermodynamic effects reduce summer warming and enhance winter warming, playing a key role for the seasonal pattern of Arctic warming across a broad range of model complexity.

c. *Mechanisms linking sea ice to seasonality in Arctic warming*

Figure 6 illustrates that one way in which sea ice thermodynamics contribute to seasonality in Arctic warming is through suppressing summer warming, consistent with the

large effective heat capacity of melting ice. Transitioning from frozen ice to open ocean would also lead to suppressed summer warming, as seen in the SCM experiments. As also seen in the SCM, enhanced early winter warming when including ice thermodynamics in the GCM is consistent with the effects of increasing conductive heat flux as ice below freezing thins, although additional climate feedbacks also contribute to winter warming in the GCM. A slight phase delay in surface temperature as ice melts and exposes open ocean under CO_2 doubling (Fig. 6a) would widen with a transition to a seasonally ice-free Arctic under greater forcing (Fig. 1), additionally supporting an early winter warming maximum as a result of effective heat capacity changes. Surface temperatures under CO_2 doubling show a larger phase delay when averaged exclusively over the sea ice edge, where the surface layer is transitioning from frozen ice to open ocean in early winter (Fig. S6). Thus, the role of sea ice thermodynamics for seasonality in warming in the GCM appears consistent with the SCM results.

In addition to these direct effects of sea ice thermodynamics, we consider indirect effects of ice thermodynamics on the seasonal pattern of warming via impacts on the lapse-rate feedback. The small effective heat capacity of frozen ice gives surface temperatures a large seasonal amplitude that brings temperatures to the freezing point in summer, where they remain due to the very large effective heat capacity of melting ice. As a result of these relatively warm summer surface temperatures, the preindustrial *Ice* experiment has weak summer stability (Fig. 7a, solid light blue line), compared to strong surface temperature inversions during winter (Fig. 7b). In contrast, the annually large effective heat capacity of the ocean surface layer in the preindustrial *No ice*, *set albedo* experiment gives surface temperatures a small seasonal amplitude, so that they remain below the freezing point in summer (Fig. 7a, dashed light blue line). This produces base-state summer inversions that, combined with the elimination of the latent energy sink of melting ice in this experiment, support stronger surface-trapped warming during summer under doubled CO_2. These results suggest that in addition to suppressing summer warming due to the large effective heat capacity of melting ice, sea ice thermodynamics may also promote seasonality in warming by inhibiting a positive summertime lapse-rate feedback.

To quantify contributions from the lapse-rate and other feedbacks to Arctic warming under CO_2 doubling, we apply the radiative kernel method using CAM3 kernels (Shell et al. 2008; Soden et al. 2008). We also calculate the annual atmospheric heat transport (AHT) convergence as the difference between surface and net TOA fluxes, and additionally subtract atmospheric energy and moisture storage to calculate the seasonal cycle of AHT convergence, following Donohoe et al. (2020a). In addition to changes in AHT under CO_2 doubling, we consider changes in the surface energy budget (SEB), which includes both ice export changes and seasonal ocean heat storage in the CESM SOM. Energetic contributions from each feedback ($\lambda_i \Delta T$), the Planck response ($\lambda_p \Delta T$), CO_2 forcing (F), changes in SEB and AHT, and a residual term (ΔR_{res}) are then converted into contributions to near-surface warming (ΔT) for the nonland Arctic based on a local energy budget [Eq. (10)], following previous studies such as Goosse et al. (2018) and Pithan and Mauritsen (2014):

$$F + \left(\lambda_p + \sum_i \lambda_i\right)\Delta T + \Delta\text{AHT} + \Delta\text{SEB} + \Delta R_{\text{res}} = 0. \tag{10}$$

Annual, summer (June–August), and winter (December–February) warming contributions are determined by dividing each term in Eq. (10), all in units of W m^{-2}, by the magnitude of the nonland Arctic Planck response in the *Ice* experiment ($\lambda_{p,\text{Ice}}$) in W m^{-2} K^{-1}:

$$\Delta T = -\frac{F}{\lambda_{p,\text{Ice}}} - \frac{\lambda_p' \Delta T}{\lambda_{p,\text{Ice}}} - \frac{\sum_i \lambda_i \Delta T}{\lambda_{p,\text{Ice}}} - \frac{\Delta\text{AHT}}{\lambda_{p,\text{Ice}}} - \frac{\Delta\text{SEB}}{\lambda_{p,\text{Ice}}} - \frac{\Delta R_{\text{res}}}{\lambda_{p,\text{Ice}}}, \tag{11}$$

where $\lambda_p' = \lambda_p - \lambda_{p,\text{Ice}}$ is the difference between the nonland Arctic Planck feedback for a given experiment, λ_p, and $\lambda_{p,\text{Ice}}$.

In Fig. 8, contributions to nonland Arctic warming in the *Ice* configuration of the CESM SOM are plotted along the horizontal axis, while contributions to warming in the *No ice*, *set albedo* configuration are plotted along the vertical axis. The albedo feedback is nearly identical by design for both experiments. Greater annual-mean warming in the *No ice*, *set albedo* experiments compared to the *Ice* experiments is mainly contributed by a more-positive lapse-rate feedback (Fig. 8a). This results from a stronger lapse-rate contribution to summer warming in the *No ice*, *set albedo* experiments (Fig. 8b), while the lapse-rate contribution to winter warming is similar for both sets of experiments (Fig. 8c). In addition to the lapse-rate feedback, negative ΔSEB due to reduced sea ice export under CO_2 doubling slightly weakens annual warming in the *Ice* experiment compared to the *No ice*, *set albedo* experiment, consistent with the SCM experiments. Seasonally, the ΔSEB contribution indicates stronger energy transfer from the atmosphere to ocean in summer and from the ocean to atmosphere in winter in the *Ice* experiment, which also contributes to stronger seasonality in warming.

The *Ice* and *No ice*, *set albedo* experiments show similar DJF warming because reduced winter ocean-to-atmosphere heat transfer in the *No ice*, *set albedo* experiment is compensated by increased winter poleward AHT. Despite reduced seasonal ocean heat storage, the winter lapse-rate feedback remains similarly strong in the *No ice*, *set albedo* experiment compared to the *Ice* experiment. In contrast to the hypothesis of Dai et al. (2019) and Chung et al. (2021), these results suggest that a strong wintertime lapse-rate feedback is possible with only the albedo effects of sea ice loss, in the absence of sea ice insulation loss.

A caveat to this feedback analysis in the *No ice*, *set albedo* experiments is that we use radiative kernels derived from experiments that include sea ice. In reality, we would expect that a colder and drier lower troposphere during summer in

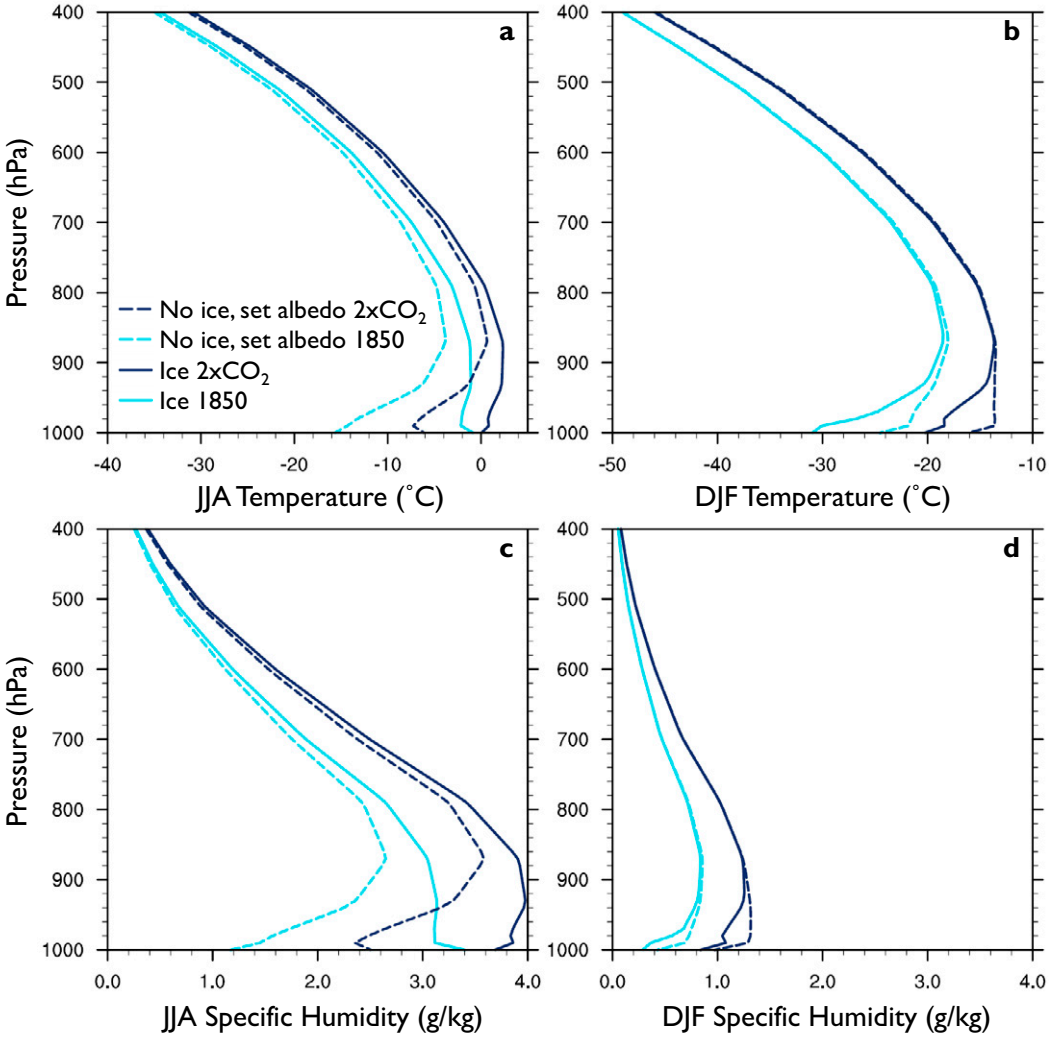

FIG. 7. (a),(b) Atmospheric temperature (°C) and (c),(d) specific humidity (g kg^{-1}) over nonland surfaces from 70° to 90°N for (a),(c) June–August (JJA) and (b),(d) December–February (DJF) in the *Ice* (solid) and *No ice*, *set albedo* (dashed) CESM SOM experiments under preindustrial conditions (light blue) and doubled CO_2 (dark blue).

the *No ice*, *set albedo* experiments (Fig. 7) would diminish the effect of atmospheric temperature changes on TOA radiation (the temperature radiative kernel), and thus lead to a weaker summer lapse-rate feedback than that shown in Fig. 8. We test the sensitivity of feedback warming contributions to this choice of radiative kernel by substituting kernels from other months and find similar results, with the lapse-rate feedback still contributing most to greater summer warming in the *No ice*, *set albedo* experiment compared to the *Ice* experiment (see supplemental text S1).

4. Summary and conclusions

We use idealized experiments with certain sea ice processes individually inactivated in a GCM as well as a simpler model in order to disentangle potential causes of seasonality in Arctic warming under CO_2 forcing. A simple SCM is able to capture key features of Arctic warming seasonality: a summer minimum and early winter maximum in Arctic warming, shifting to a late winter maximum under greater forcing. Several factors contribute to the warming seasonality in this model, including seasonality in the Planck response, albedo feedback, and conductive heat flux through ice. In the absence of seasonality in climate feedbacks, the SCM simulates peak early winter warming over ice below freezing due to increasing conductive heat flux as ice thins, while the large effective heat capacity of melting ice suppresses summer warming. When conductive heat flux variations with ice thickness are further eliminated, the SCM still exhibits peak early winter warming due to a phase delay and amplitude reduction in surface temperature as perennial sea ice transitions to a seasonally ice-free ocean. While frozen sea ice warms quickly to the melting point in summer and cools quickly to very cold winter

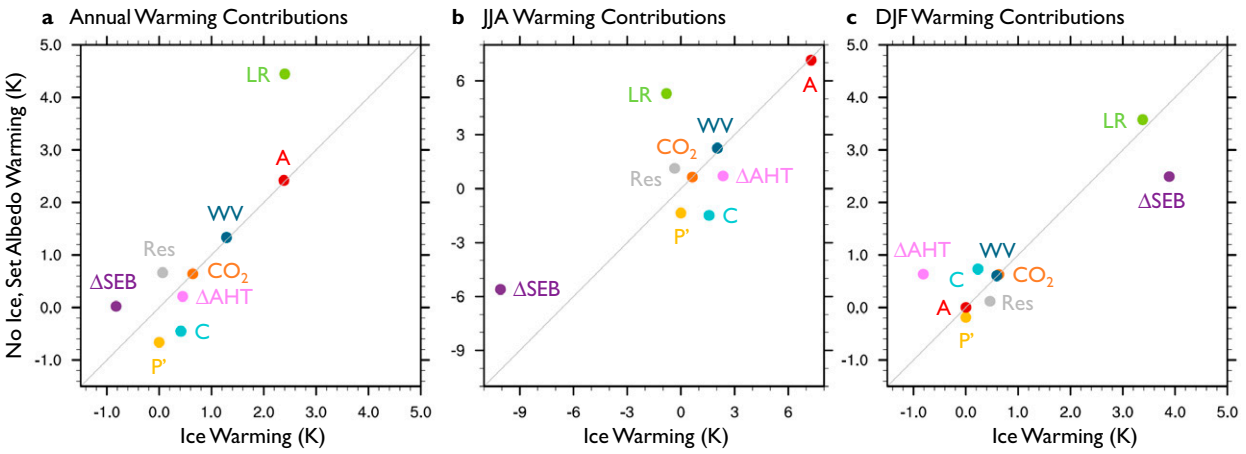

FIG. 8. Contributions to (a) annual-mean, (b) JJA, and (c) DJF warming (°C) over nonland surfaces from 70° to 90°N under CO_2 doubling in the CESM SOM in the *Ice* configuration (horizontal axis) and *No ice*, *set albedo* configuration (vertical axis). Warming contributions are shown for the lapse-rate (LR), surface albedo (A), water vapor (WV), and cloud (C) feedbacks, the variation in the Planck response from its value in the *Ice* experiment (P'), CO_2 forcing (CO_2), change in atmospheric heat transport convergence (ΔAHT) and surface energy budget (ΔSEB), which includes ice export and seasonal ocean heat storage, and residual term (Res). The total near-surface warming for the *Ice* and *No ice*, *set albedo* experiments, respectively, is 6.8 and 8.6 K annually, 2.7 and 8.7 K in JJA, and 8.4 and 8.6 K in DJF.

temperatures in the zero-forcing experiment, exposed open ocean in fall and early winter at increased forcing undergoes slower seasonal warming and cooling due to its larger effective heat capacity, keeping temperatures above freezing later in the year and supporting peak early winter warming relative to the zero-forcing experiment. With greater forcing, this transition and associated amplitude reduction from colder ice to warmer ocean temperatures occurs later in the year, producing peak warming in late winter. SCM experiments demonstrate that representing the evolving effective heat capacity of the Arctic surface layer is alone sufficient to reproduce the key features of seasonality in Arctic warming. Additional feedbacks in the SCM interact with these effective heat capacity changes by reducing the amount of forcing required to transition from frozen ice to melting ice and open ocean, supporting an increase in effective heat capacity and associated peak early winter warming under less forcing.

Consistent with the SCM results, GCM experiments with doubled CO_2 simulate peak early winter warming and weak summer warming when sea ice is included. Comparison of experiments with sea ice to those with identical, prescribed surface albedo changes but no sea ice under CO_2 forcing suggests that seasonality in Arctic warming depends on sea ice thermodynamic effects in both the SCM and GCM. Sea ice melt suppresses summer warming while winter warming is amplified by increasing conductive heat flux through thinning ice and increasing effective heat capacity as ice melts and exposes open ocean. In the GCM, sea ice also damps summer warming by inhibiting a positive summer lapse-rate feedback due to weak base-state atmospheric stability and minimal near-surface warming in the presence of summer sea ice melt. In winter, weaker seasonal ocean heat release to the atmosphere in the *No ice*, *set albedo* GCM experiments is compensated by an increase in poleward AHT. This supports similar winter warming for the *No ice*, *set albedo* and the *Ice* experiments in the GCM, as does a strong winter lapse-rate feedback with only the albedo effects of sea ice loss.

Similar to previous studies, our results support a key role of sea ice in setting the seasonality of Arctic warming. Here we highlight effective heat capacity changes as a fundamental mechanism for this seasonality in warming, with results demonstrating the utility of simpler models for understanding mechanisms of Arctic warming. Idealized GCM experiments also offer insight into the interconnected effects of sea ice on surface albedo changes, seasonal ocean heat storage, and insulation loss and their impacts on the lapse-rate feedback. These experiments suggest that a strong wintertime lapse-rate feedback can be produced with the albedo effects of sea ice loss alone, in contrast to the idea that seasonal heat transfer related to sea ice insulation loss is necessary to kick-start the winter lapse-rate feedback.

Disentangling these effects of sea ice is difficult in GCMs in part because diagnostic frameworks like warming contribution analyses implicitly include interactions between different contributors. Feedbacks such as the lapse-rate feedback are also impacted by heat capacity effects on surface warming, which are not explicitly quantified in this warming contribution framework. This limitation highlights a need for alternative frameworks, simpler models, and idealized experiments to isolate the mechanisms of polar amplification and interactions between mechanisms, as also suggested by Boeke et al. (2021) and Feldl et al. (2020). The key role of effective heat capacity changes for seasonality in Arctic warming, emphasized here with a simple model and idealized GCM experiments, also highlights a need to accurately model the transition from perennial ice to seasonally ice-free conditions in comprehensive GCMs in

order to project the timing and magnitude of peak Arctic warming.

Acknowledgments. We acknowledge high-performance computing support from Cheyenne (https://doi.org/10.5065/D6RX99HX) provided by NCAR's Computational and Information Systems Laboratory (2019), sponsored by the National Science Foundation. LCH was supported by the National Science Foundation (NSF) Graduate Research Fellowship Grant DGE-1762114 and the ARCS Foundation Fellowship. KCA was supported by National Science Foundation Grants AGS-1752796 and OCE-1850900 and an Alfred P. Sloan Research Fellowship. IE was supported by NSF OPP-1643445. CMB was supported by NSF OPP-1643431.

Data availability statement. The Eisenman and Wettlaufer (2009) single-column sea ice model is available from https://eisenman-group.github.io (sea_ice_model_EW09.m). The CESM2 1pctCO2-4xext experiments can be found in the Earth System Grid Federation (ESGF) repository at https://esgf-node.llnl.gov/projects/esgf-llnl/. Monthly climatologies of model output from idealized CESM experiments are available at https://doi.org/10.5281/zenodo.4925048.

REFERENCES

Bintanja, R., and E. van der Linden, 2013: The changing seasonal climate in the Arctic. *Sci. Rep.*, **3**, 1556, https://doi.org/10.1038/srep01556.

——, R. Graversen, and W. Hazeleger, 2011: Arctic winter warming amplified by the thermal inversion and consequent low infrared cooling to space. *Nat. Geosci.*, **4**, 758–761, https://doi.org/10.1038/ngeo1285.

Bitz, C. M., K. M. Shell, P. R. Gent, D. A. Bailey, G. Danabasoglu, K. C. Armour, M. M. Holland, and J. T. Kiehl, 2012: Climate sensitivity of the Community Climate System Model, version 4. *J. Climate*, **25**, 3053–3070, https://doi.org/10.1175/JCLI-D-11-00290.1.

Boeke, R. C., P. C. Taylor, and S. A. Sejas, 2021: On the nature of the Arctic's positive lapse-rate feedback. *Geophys. Res. Lett.* **48**, e2020GL091109, https://doi.org/10.1029/2020GL091109.

Chung, E.-S., K.-J. Ha, A. Timmermann, M. F. Stuecker, T. Bodai, and S.-K. Lee, 2021: Cold-season Arctic amplification driven by Arctic Ocean-mediated seasonal energy transfer. *Earth's Future* **9**, e2020EF001898, https://doi.org/10.1029/2020EF001898.

Computational and Information Systems Laboratory, 2019: Cheyenne: HPE/SGI ICE XA System (University Community Computing). National Center for Atmospheric Research, https://doi.org/10.5065/D6RX99HX.

Cronin, T. W., and M. F. Jansen, 2016: Analytic radiative-advective equilibrium as a model for high-latitude climate. *Geophys. Res. Lett.*, **43**, 449–457, https://doi.org/10.1002/2015GL067172.

Dai, A., D. Luo, M. Song, and J. Liu, 2019: Arctic amplification is caused by sea-ice loss under increasing CO_2. *Nat. Commun.*, **10**, 121, https://doi.org/10.1038/s41467-018-07954-9.

Danabasoglu, G., and Coauthors, 2020: The Community Earth System Model version 2 (CESM2). *J. Adv. Model. Earth Syst.*, **12**, e2019MS001916, https://doi.org/10.1029/2019MS001916.

Deser, C., R. Tomas, M. Alexander, and D. Lawrence, 2010: The seasonal atmospheric response to projected Arctic sea ice loss in the late twenty-first century. *J. Climate*, **23**, 333–351, https://doi.org/10.1175/2009JCLI3053.1.

Donohoe, A., K. C. Armour, G. H. Roe, D. S. Battisti, and L. Hahn, 2020a: The partitioning of meridional heat transport from the Last Glacial Maximum to CO_2 quadrupling in coupled climate models. *J. Climate*, **33**, 4141–4165, https://doi.org/10.1175/JCLI-D-19-0797.1.

Dwyer, J. G., M. Biasutti, and A. H. Sobel, 2012: Projected changes in the seasonal cycle of surface temperature. *J. Climate*, **25**, 6359–6374, https://doi.org/10.1175/JCLI-D-11-00741.1.

Eisenman, I., and J. S. Wettlaufer, 2009: Nonlinear threshold behavior during the loss of Arctic sea ice. *Proc. Natl. Acad. Sci. USA*, **106**, 28–32, https://doi.org/10.1073/pnas.0806887106.

Feldl, N., and T. M. Merlis, 2021: Polar amplification in idealized climates: The role of ice, moisture, and seasons. *Geophys. Res. Lett.* **48**, e2021GL094130, https://doi.org/10.1029/2021GL094130.

——, S. Bordoni, and T. M. Merlis, 2017: Coupled high-latitude climate feedbacks and their impact on atmospheric heat transport. *J. Climate*, **30**, 189–201, https://doi.org/10.1175/JCLI-D-16-0324.1.

——, S. Po-Chedley, H. K. A. Singh, S. Hay, and P. J. Kushner, 2020: Sea ice and atmospheric circulation shape the high-latitude lapse rate feedback. *npj Climate Atmos. Sci.*, **3**, 41, https://doi.org/10.1038/s41612-020-00146-7.

Goosse, H., and Coauthors, 2018: Quantifying climate feedbacks in polar regions. *Nat. Commun.*, **9**, 1919, https://doi.org/10.1038/s41467-018-04173-0.

Graversen, R. G., P. L. Langen, and T. Mauritsen, 2014: Polar amplification in CCSM4: Contributions from the lapse rate and surface albedo feedbacks. *J. Climate*, **27**, 4433–4450, https://doi.org/10.1175/JCLI-D-13-00551.1.

Hahn, L. C., K. C. Armour, D. S. Battisti, A. Donohoe, A. G. Pauling, and C. M. Bitz, 2020: Antarctic elevation drives hemispheric asymmetry in polar lapse rate climatology and feedback. *Geophys. Res. Lett.* **47**, e2020GL088965, https://doi.org/10.1029/2020GL088965.

——, ——, M. D. Zelinka, C. M. Bitz, and A. Donohoe, 2021: Contributions to polar amplification in CMIP5 and CMIP6 models. *Front. Earth Sci.*, **9**, 710036, https://doi.org/10.3389/feart.2021.710036.

Henry, M., and G. K. Vallis, 2021: Reduced high-latitude land seasonality in climates with very high carbon dioxide. *J. Climate*, **34**, 7325–7336, https://doi.org/10.1175/JCLI-D-21-0131.1.

——, T. M. Merlis, N. J. Lutsko, and B. E. J. Rose, 2021: Decomposing the drivers of polar amplification with a single-column model. *J. Climate*, **34**, 2355–2365, https://doi.org/10.1175/JCLI-D-20-0178.1.

Holland, M. M., and C. M. Bitz, 2003: Polar amplification of climate change in coupled models. *Climate Dyn.*, **21**, 221–232, https://doi.org/10.1007/s00382-003-0332-6.

Hunke, E., and W. Lipscomb, 2008: CICE: The Los Alamos Sea Ice Model documentation and software, version 4.0. Tech. Rep. LA-CC-06-012, Los Alamos National Laboratory, 72 pp., https://github.com/CICE-Consortium/CICE-svn-trunk/tree/svn/tags/release-4.0/doc.

Hurrell, J. W., and Coauthors, 2013: The Community Earth System Model: A framework for collaborative research. *Bull. Amer. Meteor. Soc.*, **94**, 1339–1360, https://doi.org/10.1175/BAMS-D-12-00121.1.

Kalnay, E., and Coauthors, 1996: The NCEP/NCAR 40-Year Reanalysis Project. *Bull. Amer. Meteor. Soc.*, **77**, 437–471,

https://doi.org/10.1175/1520-0477(1996)077<0437:TNYRP>2.0.CO;2.

Lu, J., and M. Cai, 2009: Seasonality of polar surface warming amplification in climate simulations. *Geophys. Res. Lett.*, **36**, L16704, https://doi.org/10.1029/2009GL040133.

Manabe, S., and R. J. Stouffer, 1980: Sensitivity of a global climate model to an increase of CO_2 concentration in the atmosphere. *J. Geophys. Res.*, **85**, 5529–5554, https://doi.org/10.1029/JC085iC10p05529.

Mann, M. E., and J. Park, 1996: Greenhouse warming and changes in the seasonal cycle of temperature: Model versus observations. *Geophys. Res. Lett.*, **23**, 1111–1114, https://doi.org/10.1029/96GL01066.

Maykut, G. A., and N. Untersteiner, 1971: Some results from a time-dependent thermodynamic model of sea ice. *J. Geophys. Res.*, **76**, 1550–1575, https://doi.org/10.1029/JC076i006p01550.

——, and P. E. Church, 1973: Radiation climate of Barrow, Alaska, 1962–66. *J. Appl. Meteor.*, **12**, 620–628, https://doi.org/10.1175/1520-0450(1973)012<0620:RCOBA>2.0.CO;2.

Nakamura, N., and A. H. Oort, 1988: Atmospheric heat budgets of the polar regions. *J. Geophys. Res.*, **93**, 9510–9524, https://doi.org/10.1029/JD093iD08p09510.

Neale, R. B., J. Richter, S. Park, P. H. Lauritzen, S. J. Vavrus, P. J. Rasch, and M. Zhang, 2013: The mean climate of the Community Atmosphere Model (CAM4) in forced SST and fully coupled experiments. *J. Climate*, **26**, 5150–5168, https://doi.org/10.1175/JCLI-D-12-00236.1.

Oleson, K. W., and Coauthors, 2010: Technical description of version 4.0 of the Community Land Model (CLM). NCAR Tech. Rep. TN-478+STR, 257 pp., https://doi.org/10.5065/D6FB50WZ.

Payne, A. E., M. F. Jansen, and T. W. Cronin, 2015: Conceptual model analysis of the influence of temperature feedbacks on polar amplification. *Geophys. Res. Lett.*, **42**, 9561–9570, https://doi.org/10.1002/2015GL065889.

Peralta-Ferriz, C., and R. A. Woodgate, 2015: Seasonal and interannual variability of pan-Arctic surface mixed layer properties from 1979 to 2012 from hydrographic data, and the dominance of stratification for multiyear mixed layer depth shoaling. *Prog. Oceanogr.*, **134**, 19–53, https://doi.org/10.1016/j.pocean.2014.12.005.

Pithan, F., and T. Mauritsen, 2014: Arctic amplification dominated by temperature feedbacks in contemporary climate models. *Nat. Geosci.*, **7**, 181–184, https://doi.org/10.1038/ngeo2071.

——, B. Medeiros, and T. Mauritsen, 2014: Mixed-phase clouds cause climate model biases in Arctic wintertime temperature inversions. *Climate Dyn.*, **43**, 289–303, https://doi.org/10.1007/s00382-013-1964-9.

Robock, A., 1983: Ice and snow feedbacks and the latitudinal and seasonal distribution of climate sensitivity. *J. Atmos. Sci.*, **40**, 986–997, https://doi.org/10.1175/1520-0469(1983)040<0986:IASFAT>2.0.CO;2.

Screen, J. A., and I. Simmonds, 2010a: The central role of diminishing sea ice in recent Arctic temperature amplification. *Nature*, **464**, 1334–1337, https://doi.org/10.1038/nature09051.

——, and ——, 2010b: Increasing fall–winter energy loss from the Arctic Ocean and its role in Arctic temperature amplification. *Geophys. Res. Lett.*, **37**, L16707, https://doi.org/10.1029/2010GL044136.

Sejas, S. A., M. Cai, A. Hu, G. A. Meehl, W. Washington, and P. C. Taylor, 2014: Individual feedback contributions to the seasonality of surface warming. *J. Climate*, **27**, 5653–5669, https://doi.org/10.1175/JCLI-D-13-00658.1.

Serreze, M. C., A. P. Barrett, J. C. Stroeve, D. N. Kindig, and M. M. Holland, 2009: The emergence of surface-based Arctic amplification. *Cryosphere*, **3**, 11–19, https://doi.org/10.5194/tc-3-11-2009.

Shell, K. M., J. T. Kiehl, and C. A. Shields, 2008: Using the radiative kernel technique to calculate climate feedbacks in NCAR's Community Atmospheric Model. *J. Climate*, **21**, 2269–2282, https://doi.org/10.1175/2007JCLI2044.1.

Soden, B. J., I. M. Held, R. Colman, K. M. Shell, J. T. Kiehl, and C. A. Shield, 2008: Quantifying climate feedbacks using radiative kernels. *J. Climate*, **21**, 3504–3520, https://doi.org/10.1175/2007JCLI2110.1.

Yoshimori, M., A. Abe-Ouchi, M. Watanabe, A. Oka, and T. Ogura, 2014: Robust seasonality of Arctic warming processes in two different versions of the MIROC GCM. *J. Climate*, **27**, 6358–6375, https://doi.org/10.1175/JCLI-D-14-00086.1.

Supplementary Information for **Seasonality in Arctic Warming Driven By Sea Ice Effective Heat Capacity**

Lily C. Hahn[a], Kyle C. Armour[a,b], David S. Battisti[a], Ian Eisenman[c], Cecilia M. Bitz[a]

[a]*Department of Atmospheric Sciences, University of Washington, Seattle, WA*

[b]*School of Oceanography, University of Washington, Seattle, WA*

[c]*Scripps Institution of Oceanography, University of California San Diego, La Jolla, CA*

Table S1. Model default parameter values. For seasonally varying parameters, both the annual- and monthly-mean values (starting in January) are given.

Parameter	Description	Value (annual-mean; monthly)
L_i	Latent heat of fusion for sea ice	9.5 W m^{-3} yr
c_{ml}	Ocean mixed layer specific heat capacity	0.13 W m^{-3} yr K^{-1}
H_{ml}	Ocean mixed layer depth	50 m
α_i	Ice-covered surface albedo	0.68
α_{ml}	Surface albedo of ocean mixed layer	0.2
k_i	Thermal conductivity of sea ice	2 W m^{-1} K^{-1}
F_B	Basal heat flux	2 W m^{-2}
H_α	Ice thickness parameter for smooth transition from α_i to α_{ml}	0.5 m
v_0	Ice export parameter	0.1 yr^{-1}
$F_0(t)$	Temperature-independent outgoing longwave radiation flux	85 W m^{-2}; (120, 130, 140, 95, 63, 60, 56, 52, 54, 63, 81, 110) W m^{-2}
$F_T(t)$	Temperature-dependent outgoing longwave radiation flux	2.8 W m^{-2} K^{-1}; (3.2, 3.2, 3.4, 2.9, 2.6, 2.6, 2.6, 2.5, 2.5, 2.6, 2.7, 3.1) W m^{-2} K^{-1}
$F_S(t)$	Incident shortwave radiation flux	100 W m^{-2}; (0, 0, 30, 160, 280, 310, 220, 140, 59, 6.4, 0, 0) W m^{-2}
ΔF_0	Imposed surface forcing	0 W m^{-2}
λ_{LR}	Annual- and monthly-mean lapse-rate feedback added in Section 2f, averaged over non-land Arctic gridpoints that remain below freezing in CESM CO_2 doubling experiments	1.0 W m^{-2} K^{-1}; (1.0, 1.0, 0.9, 0.9, 0.6, NaN, NaN, 0.7, 1.4, 1.4, 1.3, 1.1) W m^{-2} K^{-1}

Text S1. Kernel sensitivity test for the *No ice, set albedo* experiments

To test the sensitivity of feedback warming contributions in summer to the choice of radiative kernels for the *No ice, set albedo* experiments, we apply radiative kernels for the month of October to the months of June, July, and August to calculate longwave feedbacks. October near-surface temperature and specific humidity in the *Ice* experiment are more comparable with summer pre-industrial conditions in the *No ice, set albedo* experiment, although October in the *Ice* experiment is much colder and drier aloft (Figure S7). Summer feedback calculations with the October kernels should therefore give underestimated longwave feedbacks, but provide a useful kernel sensitivity test in comparison with the potentially overestimated longwave feedbacks shown in Figure 8. For the shortwave feedbacks, we apply the approximate partial radiative perturbation method of Taylor et al. (2007) as an alternative to the kernel method. The results of these alternative feedback calculations are shown in Figure S8. Although the summer lapse-rate feedback contribution for the *No ice, set albedo* experiment is slightly reduced, warming contributions are largely similar to those shown in Figure 8, and the lapse-rate feedback still contributes most to greater summer warming in the *No ice, set albedo* experiment compared to the *Ice* experiment.

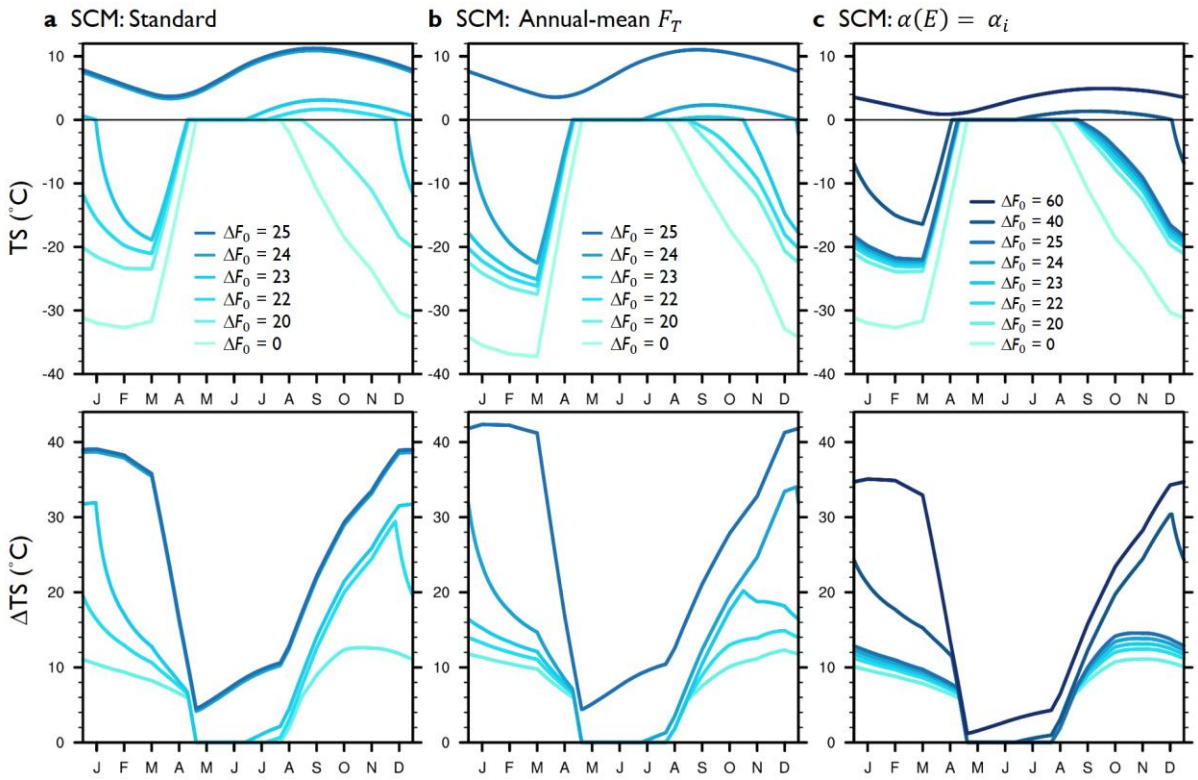

Figure S1. Surface temperature (TS; ˚C) for surface forcing experiments in (a) the standard SCM, (c) the SCM with annual-mean $F_T(t)$, and (c) the SCM with constant $\alpha(E) = \alpha_i$. The bottom row shows TS anomalies compared to the ΔF_0 = 0 experiment.

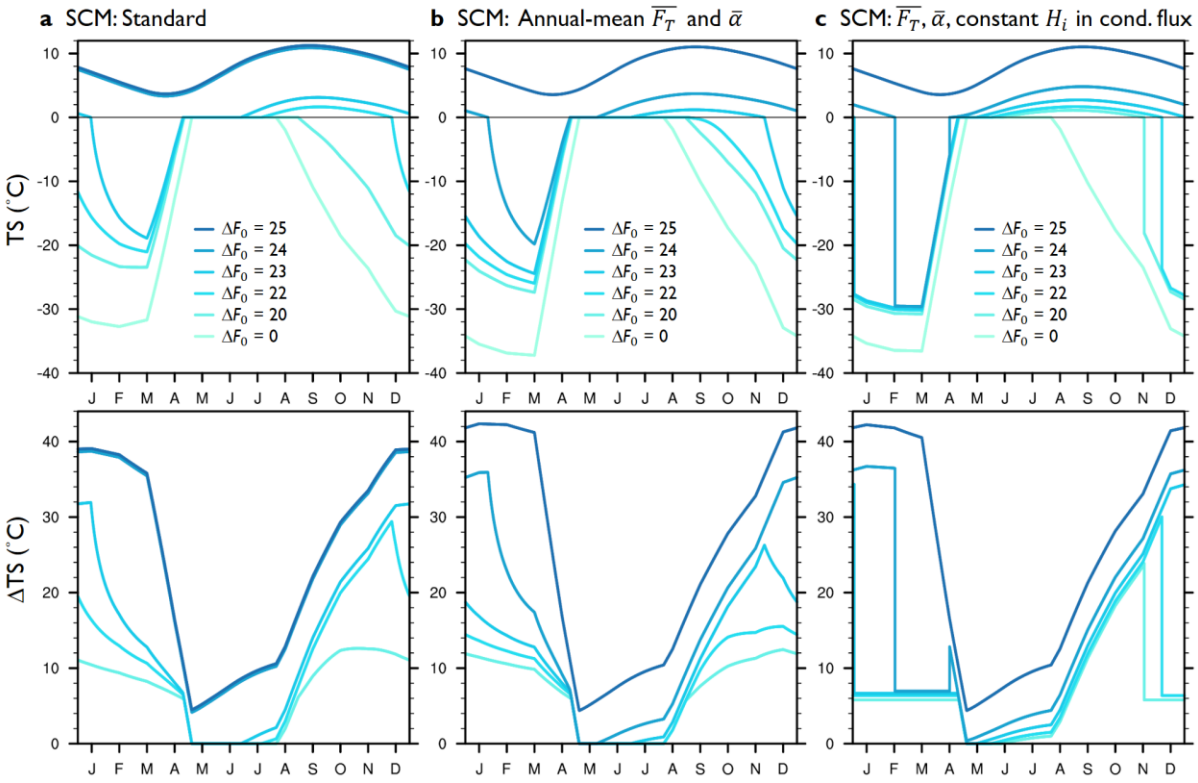

Figure S2. Surface temperature (TS; ˚C) for surface forcing experiments in (a) the standard SCM, (b) the SCM with annual-mean $F_T(t)$ and annual-mean $\bar{\alpha}$, which is set to the annual-mean albedo from each forcing experiment with annual-mean $F_T(t)$ (thus eliminating seasonality in the albedo feedback while maintaining an annual-mean albedo feedback), and (c) the SCM with annual-mean $F_T(t)$, annual-mean $\bar{\alpha}$, and constant ice thickness H_i when calculating the conductive heat flux through frozen ice, which is set to the annual-mean H_i from the ΔF_0 = 0 experiment with annual-mean $F_T(t)$ and annual-mean $\bar{\alpha}$. The bottom row shows TS anomalies compared to the ΔF_0 = 0 experiment.

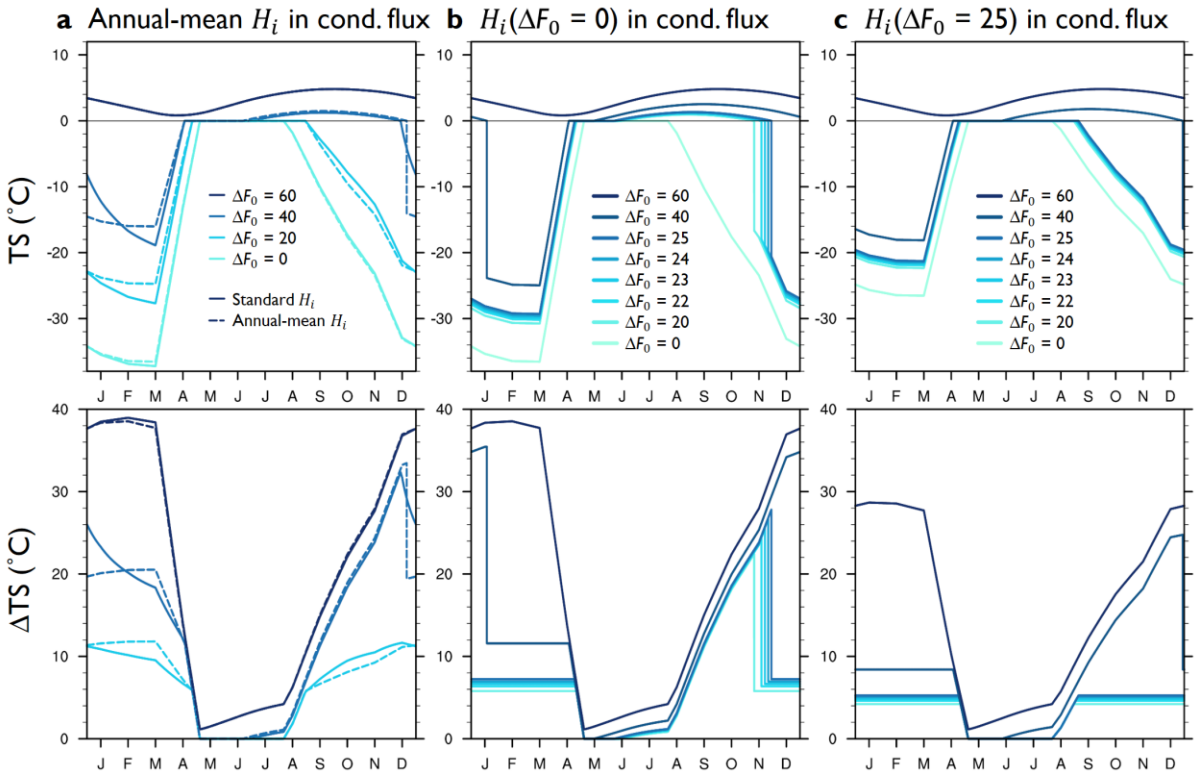

Figure S3. As in Figure 2d, surface temperature (TS; ˚C) for surface forcing experiments in the SCM with annual-mean $F_T(t)$ and constant $\alpha(E) = \alpha_i$ (a; solid lines), and constant ice thickness H_i when calculating the conductive heat flux through frozen ice, which is set to the annual-mean H_i from (a; dashed lines) each forcing experiment, (b) the $\Delta F_0 = 0$ experiment (H_i = 3.2 m) and (c) the $\Delta F_0 = 25$ experiment (H_i = 1.0 m) with annual-mean $F_T(t)$ and constant $\alpha(E) = \alpha_i$. The bottom row shows TS anomalies compared to the $\Delta F_0 = 0$ experiment.

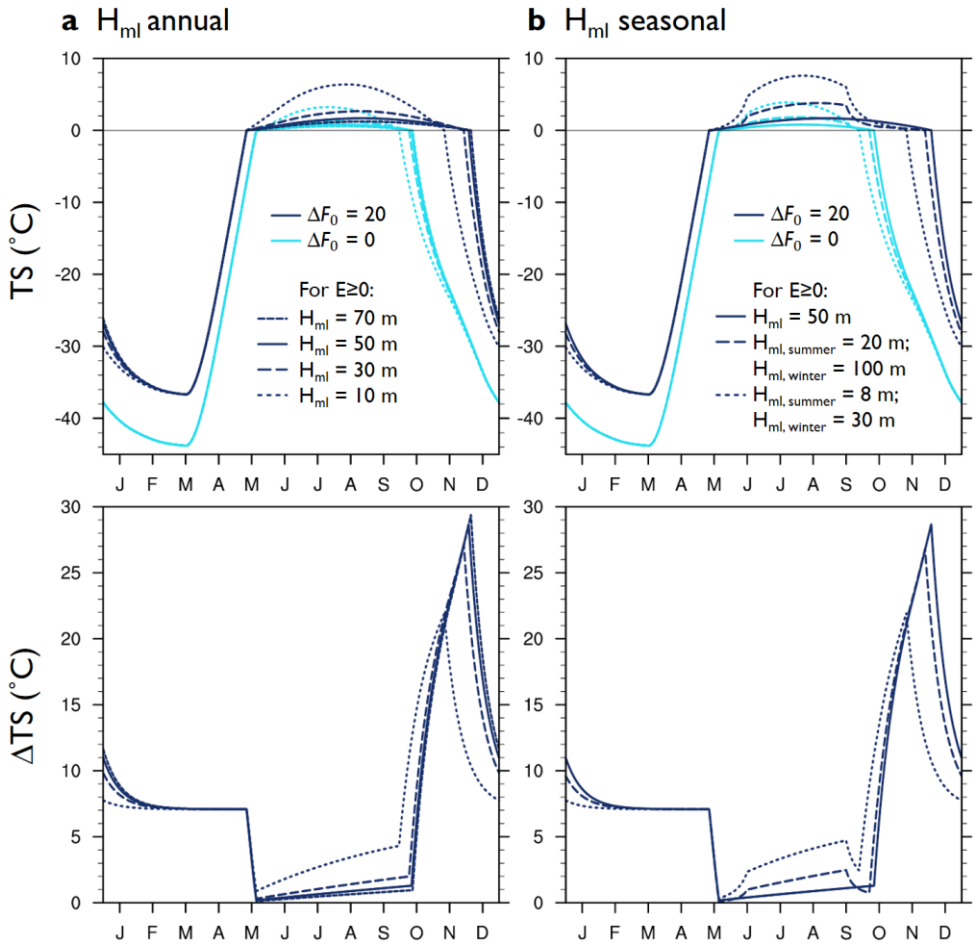

Figure S4. Surface temperature (TS; ˚C) for various surface forcings and mixed-layer depths in the SCM run as a mixed layer with annual-mean $F_T(t)$ and constant $\alpha(E) = \alpha_i$. For all cases, H_{ml}(E<0) = 1 m to represent the small effective heat capacity of sea ice, while H_{ml}(E≥0) is (a) set to various annual-mean values or (b) set to one value in summer (June-September) and another value in winter (October-May), based on observational mixed layer depths in the Eastern Arctic ($H_{ml,summer}$ = 20 m; $H_{ml,winter}$ = 100 m) or Western Arctic ($H_{ml,summer}$ = 8 m; $H_{ml,winter}$ = 30 m) taken from Peralta-Ferriz and Woodgate (2015).

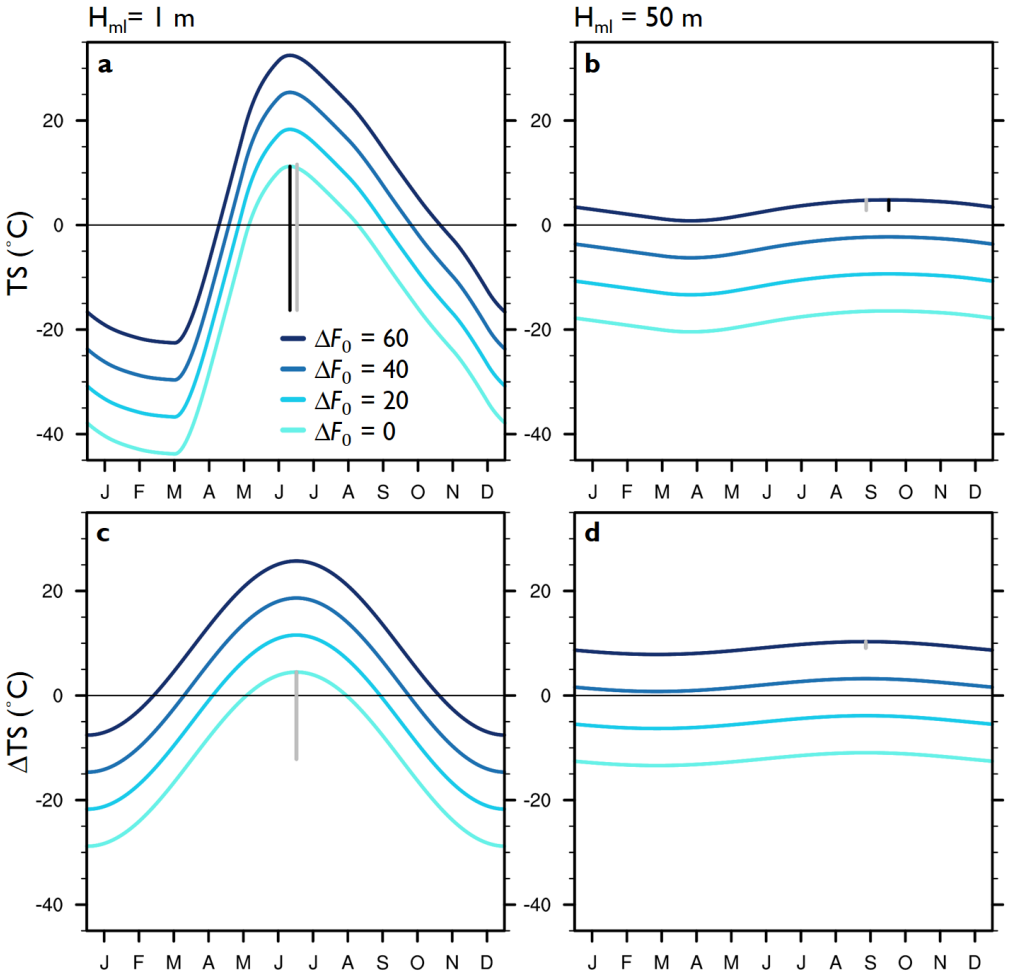

Figure S5. As in Figure 3a,b top, for (a,b) the mixed-layer SCM with annual-mean $F_T(t)$ and constant $\alpha(E) = \alpha_i$, and (c,d) the same model, but with sinusoidal solar forcing $F_s(t)$ and annual-mean $F_0(t)$. The black vertical lines indicate the timing and amplitude of maximum surface temperature for the SCM, while the grey lines show the analytical solution. Following Eq. (6) and (7), the phase shift and amplitude of surface temperature are identical for all values of ΔF_0, which is annually-constant and does not affect the seasonal amplitude of the surface forcing.

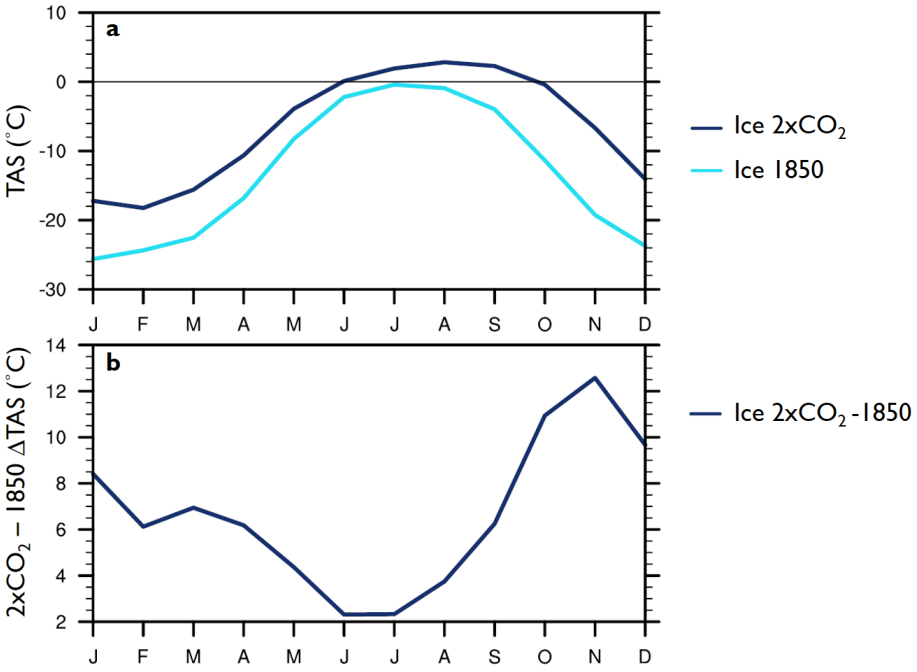

Figure S6. As in Figure 6, near-surface temperature (TAS; ˚C) over non-land surfaces from 70-90˚N for the CESM SOM *Ice* experiment under (a) pre-industrial (light blue) and doubled CO_2 (dark blue), and (b) TAS anomalies for doubled CO_2 compared to pre-industrial experiments. Here, the area average is limited to only those gridpoints with October sea-ice concentration greater than 15% under pre-industrial forcing and less than 15% under doubled CO_2.

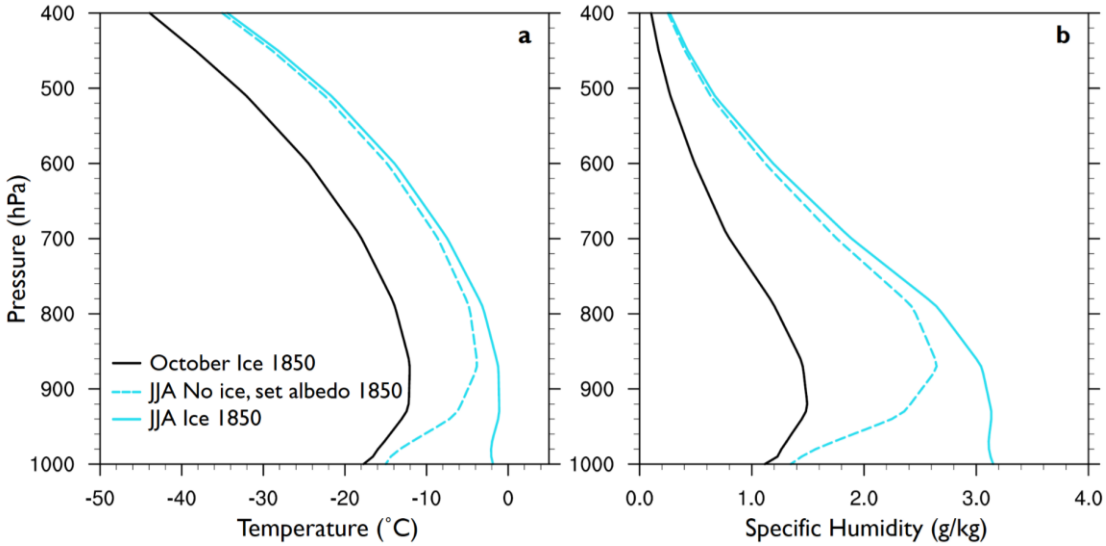

Figure S7. (a) Atmospheric temperature (˚C) and (b) specific humidity (g/kg) over non-land surfaces from 70-90˚N under pre-industrial forcing in the *No ice, set albedo* experiment during June-July-August (JJA; dashed light blue) and in the *Ice* experiment during JJA (solid light blue) and October (black).

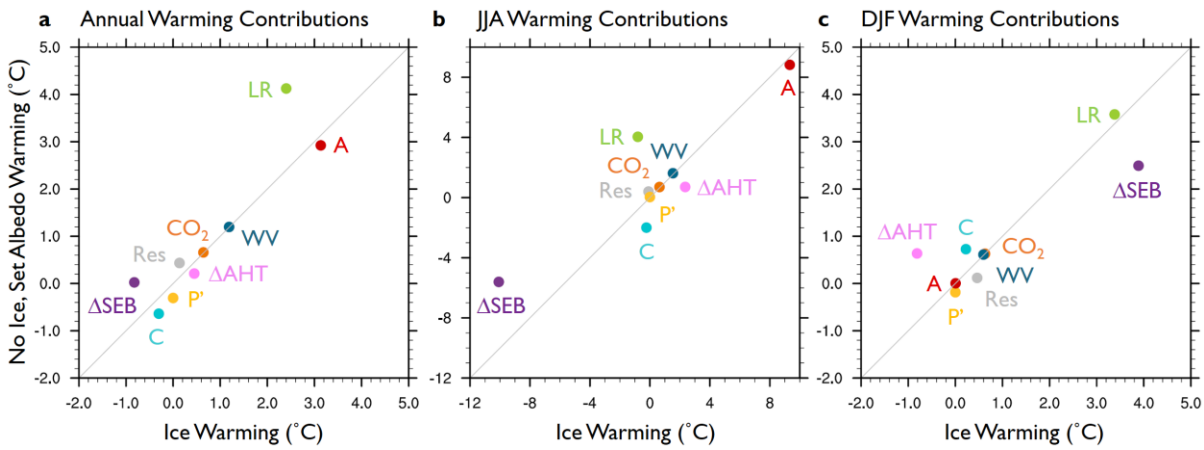

Figure S8. As in Figure 8, but using October radiative kernels to calculate JJA longwave feedbacks and using the APRP method to calculate all shortwave feedbacks: contributions to (a) annual-mean, (b) JJA, and (c) DJF warming (˚C) over non-land surfaces from 70-90˚N under CO_2 doubling in CESM *Ice* and *No ice, set albedo* experiments. Warming contributions are shown for the lapse-rate (LR), surface albedo (A), water-vapor (WV), and cloud (C) feedbacks, the variation in the Planck response from its value in the *Ice* experiment (P'), CO_2 forcing (CO_2), change in atmospheric heat transport convergence (ΔAHT) and surface energy budget (ΔSEB), which includes ice export and seasonal ocean heat storage, and residual term (Res).